Integral Mobile-fuel Fast Reactor (IMFR)

W. Van Snyder
van.snyder@sbcglobal.net

August 1, 2026

Abstract

The Integral Fast Reactor (IFR) concept is extended to the Integral Mobile-fuel Fast Reactor (IMFR), a sodium-cooled, pool-type "walk-away" safe reactor with an on-site fuel processor. Key innovations include metallic fuel particles forming a paste with sodium, continuous circulation internally and to the fuel processor (even during shutdown), and continuous fission gas removal. Fuel-cladding chemical and mechanical interactions (FCCI/FCMI) are effectively eliminated. Forty-year fuel element lifetimes with internal module replacement enable century-scale operation.

Safety is enhanced by the paste's superior thermal conductivity, even compared with solid metallic slugs, which lowers peak fuel temperatures and increases Doppler margin, combined with strong negative reactivity feedback from rapid axial thermal-hydraulic expansion. The on-site fuel processor is small, continuous, automatic, and pyrochemical, producing compact segregated mineral and metallic waste forms. A quantitative 840 MWth example is presented.

The autonomous closed IMFR fuel cycle with minimal external dependencies is a promising evolution of sodium-cooled fast reactor technology.

More importantly, the IMFR concept addresses two frequently unaccounted and intractable system-wide challenges: long-term fuel availability and waste management.

Introduction

The concept of the Integral Mobile-fuel Fast Reactor (IMFR) evolves the Integral Fast Reactor (IFR) philosophy [48]. By combining a mobile-fuel sodium-cooled, pool-type reactor with an on-site continuous fuel processor, the IMFR seeks to enhance safety, operational flexibility, and fuel-cycle autonomy while minimizing external dependencies. It also produces a much smaller waste stream consisting almost entirely of mineralized or metallic fission products.

The central enabling innovation is the integration of 50 µm metallic fuel particles with sodium to form a $\approx 78\%$ volume-mixing-ratio paste [43], together with continuous circulation of this fuel — both within each fuel element [44] and to the on-site processor as a dilute $\approx 7.8\%$ slurry — even during shutdown. Compared to traditional solid-fuel fast reactors, the approach offers several advantages:

- Fuel-cladding chemical and mechanical interactions (FCCI and FCMI) are effectively eliminated.

- Passive safety is enhanced by the paste's superior thermal conductivity, and strong negative reactivity feedback due to rapid axial thermal-hydraulic expansion and increased Doppler margin.
- Forty-year fuel element lifetimes and modular replacement support century-scale plant operation.

Given the novel nature of the mobile-fuel slurry architecture, this study is exploratory. While the system relies on technologies that require experimental verification and further development, it establishes the fundamental scaling relationships and thermodynamic principles necessary for feasibility assessment. Quantitative examples using an 840 MWth reference are intended as a design basis for identifying critical trade-offs rather than definitive engineering conclusions.

The remainder of this monograph describes the reactor core and fuel elements (Part I), the on-site fuel processing system (Part II) , and conclusions with future work (Parts III and IV).

Part I
The Reactor

The reactor described herein extends fundamental design principles of Experimental Breeder Reactor II (EBR-II) [32]. Like EBR-II, it is a "walk-away" safe sodium-cooled, pool-type reactor. Beyond EBR-II, important fundamental changes in detail are incorporated.

I.1 Fuel Elements

I.1.1 Fuel Element Design Principles

Important differences compared to those in EBR-II include:

- Fuel elements are intended to remain within the reactor core for forty years, instead of three to four years.
- Instead of solid metal slugs, fuel consists of a sodium paste of metallic particles that follow a log normal size distribution with $\mu \approx 50\,\mu m$. The random-close-packing volume mixing ratio with uniform size particles is 64%, but increases as σ increases [19, 37, 24, 43]. With $\sigma \approx 0.75$ to 0.77 the volume mixing ratio is $\approx 78\%$ [19, Fig. 1]. A log normal size distribution is a natural consequence of most particle fabrication methods.
- Rather than fuel being enclosed in pins containing sodium for thermal bond, with coolant flowing around them, it is enclosed in fuel elements penetrated by coolant tubes.
- Fuel is continuously circulated with an internal "turn over" period of $\approx 5\,h$ using eductors or "jet pumps" integrated into each fuel element [44], powered by liquid sodium to create a circulating $\approx 7.8\%$ slurry.

- Continuous gas control regulates the pressure within fuel elements to remain the same as the pressure in the surrounding medium. Fuel-element strain, the hazard of pressure-induced fuel pin rupture, and coolant duct deformation — limiting factors on fuel element residence time within EBR-II — are eliminated [48].

- Fission-product gases and fission-product neutron poisons are continuously removed because gases continuously escape through the interconnected porosity of 50 µm irradiated fuel particles and fuel is continuously circulated to the integrated fuel processor described in Part II. Gas management and fuel circulation continue during shutdown.

  Although significant reactivity transients and "restart lockouts" occur in fixed-fuel thermal-spectrum reactors due to the $^{135}\text{Te} \rightarrow ^{135}\text{I} \rightarrow ^{135}\text{Xe}$ "iodine pit," the problem does not occur in IMFR because in a fast neutron spectrum the neutron absorption cross section for ^{135}Xe is orders of magnitude smaller. Gas management does not address this operational non-problem, but it does reduce the activity load that would present a hazard in the unlikely event of a catastrophic accident.

- The $\approx 78\%$ volume mixing ratio paste of particles mixed with sodium has significantly higher thermal conductivity than solid metal slugs at all operating temperatures (Appendix E) [21, 27]. The lower operating temperature of $\approx 930\,\text{K}$ (Section I.1.5) allows a reduced TRU fuel fraction and provides more available Doppler margin for self termination. Resiliency in the face of unexpected transients such as loss of secondary coolant flow, loss of heat sink, or sudden change in reactivity is increased.

- Mobile fuel expands axially and rapidly as temperature increases, adding substantial transient thermal-hydraulic negative reactivity worth (see Section I.8.1).

- Fuel/structure chemical interaction is effectively eliminated by fuel mobility. The formation of structure-fuel eutectics that weakened fuel pin cladding — another limiting factor on fuel element residence time within EBR-II — requires prolonged contact between fuel and structure. With $\approx 5\,\text{h}$ turnover in each fuel element, prolonged contact is not possible.

The overall organizational principles are adopted from EBR-II [32, 48] and GE Vernova PRISM designs, e.g., [49]. Many high-level parameters, including the nominal 840 MWth power rating and coolant temperatures, are adopted to provide a consistent and realistic scaling basis. Assuming $\approx 37\%$ thermal efficiency leads to 310 MWe. Quantities are intended to be illustrative of a PRISM-scale plant, but are not definitive. Final engineering design will certainly result in changes, but probably not large changes.

I.1.2 Fuel Element Structure

Each fuel element is a hexagonal cylinder, or more properly a prism, with outside edge-to-edge dimension $\approx 155\,\text{mm}$ ($W \approx 89\,\text{mm}$ in Figure I.1). This dimension results from reducing the number of rings in the PRISM design from 9 to 5, and lengthening the fuel zone in each fuel element about 60% [23, Table 2]. Fuel elements are formed from RAFM — reduced activation ferritic martensitic steel (12Cr-1.5W-0.3V-0.08Ta-0.05Ti) — which is of particular interest in the fusion community. It is proposed here because of its superior resistance to abrasion rather than its reduced neutron activation.

Each fuel element consists of a fuel zone above a neutron shield and reflector. It is penetrated by vertical hexagonal coolant tubes arranged on a uniform hexagonal lattice. The number of coolant tubes is in the range 127–271 ($3\,n\,(n-1)+1$, where n is the number of tubes on each edge). A simple example with only nineteen tubes is shown in Figure I.1. Fewer coolant tubes are larger and easier to fabricate, with larger spaces between, but operating temperatures are higher with the same fuel volume fraction (Table I.4). With 271 coolant tubes, each one has a 3.125 mm internal edge-to-edge width and 0.6 mm wall thickness ($\omega = 2.5$ mm in Figure I.1). Center-to-center spacing between tubes, or pitch, is ≈ 9 mm ($s+2\omega$ in Figure I.1). The minimum inter-tube clearance is ≈ 2.7 mm so the minimum gap is ≈ 50 times the diameter of fuel particles (their edges are parallel to the duct edges, so they are corner-to-corner one to another). Fuel particles therefore do not bridge or clog between coolant tubes.

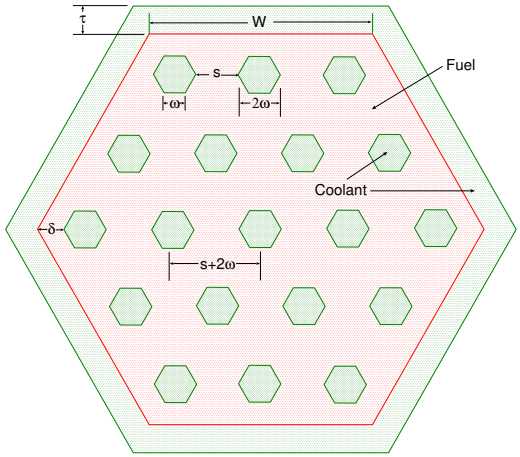

Figure I.1: Fuel element with only nineteen coolant tubes

The six outer edges are 4.5 mm thick. This robust dimension is necessary because sections optimized for twenty year service would not withstand forty years of continuous mechanical, thermal, neutronic, hydraulic, and abrasive stress. Thinner sections would exhibit insufficient margins against creep. The slightly larger initial capital expense results in lower lifetime cost.

Fuel elements are formed by hot isostatic pressing (HIP). HIP bonding is preferred to welding because it forms a diffusion bond with uniform crystal and grain structure. All internal channels are formed by machining or etching half-channels in separate sheets before HIP bonding. This is well-developed technology [26, 47, 34].

The fuel region contains four zones:

- A gas plenum 22 mm high. Fission gases are collected in and removed from this plenum. In PRISM the plenum is 1.5 times the active core length. Scaled to IMFR, that would be 1.7 m [49, § II.B].
- A sodium-filled fuel return zone 60 mm high. There is slight turbulence from fuel injection, but there is a quiet zone at least 50 mm thick.
- A settled bed of $\approx 78\%$ volume mixing ratio fuel paste, 1500 mm deep at its center and 1644 mm deep at the corners.
- A six-bin hexagonal hopper, 144 mm high at its apex.

There are three channels in each corner:

≈ 1.5 mm^2: In three corners they are used to remove fission gases by sweeping a diluent such as argon, and to regulate pressure. The other three provide sodium motive power from the maintenance crane to hydraulic actuators.[1]

[1] Hydrocarbon hydraulic fluids are quickly destroyed in a high-radiation environment.

$\approx 2.75\,\mathrm{mm}^2$: Upwardly flowing $\approx 7.8\%$ fuel slurry; the 1.88 mm diameter is >35 times the 50 µm particle diameter, so there is no danger of clogging or bridging.

$\approx 2.75\,\mathrm{mm}^2$: Downwardly flowing sodium.

Fission gas is removed from the ≈ 22 mm plenum through the central lumens of three corner splines. The gas capillaries extend into the top plate and return through 180° U-turns, integrated into the top plate, that prevent sodium from entering in the unlikely event of sloshing or gas pressure loss during an intense and prolonged earthquake. The plenum is much taller than needed for this duty: It provides space for paste to expand during rapid temperature increases, as explained in Section I.8 below. These lumens also serve to regulate pressure within the fuel element, eliminating the primary driver of creep-rupture.

The active fuel region contains ≈ 22.6 liters of $\approx 78\%$ volume mixing ratio fuel. The density of fuel alloy is $\approx 17\,\mathrm{g\,cm^{-3}}$. When fission gas production increases porosity to 25%, the fuel particle density is reduced to $\approx 12.7\,\mathrm{g\,cm^{-3}}$. The paste density is reduced from $13.4\,\mathrm{g\,cm^{-3}}$ $10.1\,\mathrm{g\,cm^{-3}}$. The mass of paste of fresh fuel in each element is ≈ 291 kg, reduced to ≈ 228 kg as burnup proceeds. The fuel volume fraction is $\approx 53\%$. As burnup increases, it is necessary to increase the fissionable isotope content to compensate for lower fuel density.

The floor of the active fuel region of each fuel element is a six-bin hexagonal hopper with its apex at the center, valleys sloping $\geq 60°$ to each corner, and a horizontal ridge to the center of each edge. The apex is 144 mm above the valley at the corner. Although there are coolant tubes along the bottom of each valley, their corner-in-valley instead of flat-in-valley orientation, together with the 60° slope and the weight of paste above the corners, conspire to prevent the formation of dead zones.

All interior surfaces are coated with W-10Ta using chemical vapor deposition to reduce abrasive wear before being assembled into the duct (Stellite cannot be applied by CVD).

The neutron shield and reflector below the hopper is formed by additive manufacturing or *binder jetting* using W-15Cr-8Fe-5Hf particles to incorporate 271 coolant passages [25]. The block is sintered to a final density of $\approx 85\%$ with final dimensions slightly less than the interior of its region in the fuel element, and coolant passages slightly larger than 3.125 mm. The hafnium fraction is a gradient, not a constant, to provide more reflection at the top, and more absorption at the bottom. Blending elemental tungsten powder with pre-alloyed Fe-Cr-Hf powder prevents the density from increasing and the block from shrinking during HIP because elemental tungsten forms a sintered skeleton that resists creep at HIP temperature (it is conjectured, but needs to be verified, that the density limit is $\approx 92\%$). Industry-standard methods are used to prevent bonding when the structure is assembled using HIP. During operation, primary coolant infiltrates, increasing thermal conductivity and providing thermal bond to the structure walls. The bottom extends ≈ 30 mm below the mounting shoulder in the grid plate. The center is a rounded blunt shape that gradually becomes a six-facet pyramid parallel to and a few millimeters above the mounting shoulder, which has the same slope as the pyramid. Coolant is admitted from this gap through holes in the duct wall to the space between elements.

A similar neutron shield could be added above the element, either integrated or as a detachable "snap on" canister. This would increase total element reactivity, which would allow a lower concentration of fissionable atoms in the fuel alloy, at the expense of taller fuel elements and a deeper containment vessel. Its corners would contain only the gas and hydraulic management capillaries.

Each fuel element is locked to the grid plate against the pressure of primary coolant flow by twelve horizontal "deadbolt" pins in the hydraulic-interface plug at the bottom of each edge of the element, described in Section I.1.3 below, one extending from each end of the plug into the grid plate. The pins are spring loaded and normally lock into the engaged position. They are disengaged using hydraulic force provided by the maintenance crane through corner channels when it connects to the element.

The vertical structure of a fuel element is summarized in Table I.1.

Table I.1: Fuel Element Vertical Structure

Elevation (mm)	**Description**
1800	Top of gas plenum, cover and tube plate.
1778	Top of 60 mm sodium clarifying zone and overflow into downcomers.
1718	Top of settled fuel bed and return of $\approx 7.8\%$ slurry.
218	Apex of floor hopper and top center of shield region.
74	Bottom corner of floor hopper.
0	Interface shoulder between fuel element and base plate.
-30	Bottom of the nose of the neutron shield.

I.1.3 Fuel Micro-Loop Circulation

A $\approx 7.8\%$ slurry (arbitrarily chosen as $\approx 10\%$ of paste VMR) circulates at the rate of $\approx 45\,\mathrm{L\,h^{-1}}$ within each fuel element, or $\approx 7.5\,\mathrm{L\,h^{-1}}$ in each corner of each fuel element, providing 5 h turnover. Fuel slurry is circulated from the bottom to the top where fuel particles are separated from sodium by gravitational settling. The $\approx 78\%$ settled paste flows passively under the influence of gravity from where it is introduced at the top, to the bottom, where it is collected and circulated back to the top as a slurry [44, 6]. Clarified sodium overflows into $2.5\,\mathrm{mm^2}$ channels within the corners and returns to the motive power sodium circulation.

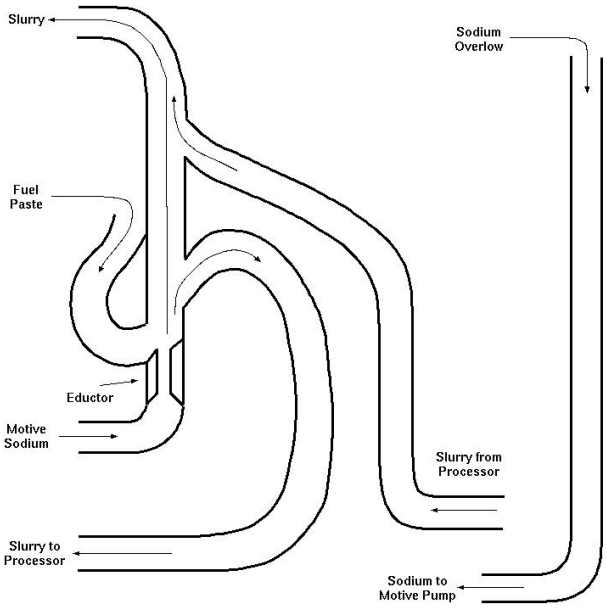

Figure I.2: Eductor and Circulation

Within each corner of the outer wall there are three channels described above. The $1.5\,\mathrm{mm^2}$ gas and hydraulic channels extend all the way to the bottom. In the vertical range beside the neutron shield, the upcomer channel is replaced by the eductor system that uses a jet of sodium. This system involves four flows: motive sodium, a bleed of 10% of the eductor's outflow diverted to the fuel processor, a return venturi for fresh fuel returning from the fuel processor, and the $\approx 7.8\%$ slurry. This entire structure is contained in the corner within a 120° teardrop with a 6 mm inner clearance around the eductor assembly.

Motive power is provided by electromagnetic pumps in the grid plate. This flow is entirely independent from primary coolant, and therefore coolant is not contaminated by fission gases, fines, or sodium-soluble fission products.

Each eductor is oriented vertically within the corner. It is positioned above an elbow within the edge, that receives motive power sodium from horizontal flow in the grid plate.

Fuel paste flows downward within the teardrop, around a sleeve around the eductor, to its intake. At the intake it flows inwardly (toward the center of the element), then outwardly through a bowl that surrounds the eductor where the central nozzle produces a high-velocity jet of sodium that "strips off" and entrains particles from fuel paste at the center of the annular suction eye to form a $\approx 7.8\%$ slurry flowing upwardly at $7.5\,\mathrm{L\,h^{-1}}$.

Above the eductor a tangential diverter extracts 10% of the developed slurry for transport to the fuel processor. This flow enters a 270° turn to change the flow from upward to downward to horizontal to join the flow to the fuel processor.

Above the outgoing-fuel diverter a venturi receives $\approx 7.8\%$ slurry from the fuel processor, arriving from an elbow. The outgoing and incoming flows are balanced so there is no system-wide concentration of material, pressure, or velocity. Positioning the return above the extraction point avoids a "short circuit" of fuel returning from the processor being immediately diverted back to the processor.

Above the venturi the flow converges through an acceleration zone to the $2.5\,\mathrm{mm^2}$ upcomer channel within the corner, wherein final mixing produces a homogeneous slurry. Flows are illustrated in Figure I.2.

The structure of this assembly is summarized in Table I.2.

Table I.2: Vertical Map of the Eductor Assembly

Altitude	Activity
0-60	Motive power elbow.
60-100	Vertical eductor nozzle.
100-130	Outgoing slurry bleed.
130-170	Return venturi.
170-216	Initial acceleration zone.
216-1778	Mixing occurs during the lift to the top.

Returning fuel to the top corners would result in a stagnant center zone. Two elbows turn the flow horizontal, then inward and sloping downward to the center through an alley between coolant tubes (see Figure I.1). This structure is supported by a "spider web" around coolant tubes.

Details of central slurry distribution will be determined by experiment. As fuel reaches orifices, back pressure provides rapidly increasing hydraulic impedance. Upflow to the top of the settled fuel bed decreases until the deposition rate equals the settled bed recession rate. Entrainment of fuel returning from the processor decreases, while the bleed to the processor loop increases. The top of the bed maintains the desired level. Fuel depth oscillations, if any, are strongly damped, with very low frequency and very small amplitude.

The difference in hydraulic impedance between partially and completely filled elements creates a self-equalizing effect. When the total fuel amount is equal to total capacity, all elements reach

a uniform fill depth. With less fuel, intentionally different characteristics in different grid plate zones preferentially fill central elements. The reactor maintains a stable, center-peaked radial power profile, allowing for passive control of total reactivity and power by adjusting fuel inventory. Excess fuel is automatically diverted to the storage annulus described in Section I.7.

The 60 mm quiet zone above the slurry return prevents a "hydraulic short circuit" of fuel particles returning in sodium overflow — and interfering with motive sodium flow — instead of settling to the fuel bed. Sodium overflows from the top of the quiet zone into intakes in the 2.5 mm^2 downflow channels in the corners, ≈ 60 mm above settled fuel. Below each overflow a horizontal (or slightly reflux) baffle extends a few millimeters inward to reduce the possibility to entrain particles. Radial vanes atop the baffle suppress a vortex, to prevent entraining cover-gas bubbles. Gas pressure and sodium flow rate measurements allow the total amount of sodium in the system to be adjusted to maintain correct levels.

The downwardly-flowing 2.5 mm^2 corner channels connect through elbows to the motive sodium flow in the grid plate.

All turns are *tractrix* turns defined parametrically as $y = a\,\mathrm{sech}(t)$, $x = y + a(t - \tanh(t))$, along which an object moves under the influence of a pull from a point moving along a straight line, where the distance between the object and the moving point remains constant. This geometry minimizes abrasion and pressure spikes [40].

A hydraulic-interface plug centered along the bottom edge of each wall contains the ends of all the bottom elbows. It fits into a socket in the grid plate to connect its channels to channels in the grid plate. This arrangement allows two-dimensional rather than three-dimensional channel systems in fuel elements and the grid plate.

Pins extending upward from the grid plate open vertical spring-loaded low-adhesion tapered sleeve valves in the plug when the element is inserted into the grid plate; they are closed by their springs when an element is removed. Normally-closed spring-loaded vertical sleeve valves within the grid plate at the ends of the hydraulic-interface socket open when the element is inserted. The three gas capillary channels connect to channels in the grid plate, with normally-closed poppet valves in both the channels and grid plate that open when the element is inserted. The hydraulic lock control channels are entirely within the fuel element.

I.1.4 Fuel Element Instrumentation

Electrical connections to fuel elements, for example for thermocouples, are undesirable, and perhaps impossible, even with "wipe clean" connectors. Non-electrical temperature and pressure sensors are necessary. In addition to the gas, upcomer, and downcomer channels, each corner includes a small lumen containing fiber Bragg grating (FBG) temperature and pressure sensors. Closely-spaced temperature sensors at the top measure the levels of the sodium-gas and fuel-sodium interfaces, while pressure sensors at the bottom indirectly measure the hydraulic impedance. Imbalances within or between fuel elements are symptoms of plugged orifices.

The FBG fibers are optically coupled to a fiber trunk below the grid plate by ceramically mounted "wipe clean" sapphire windows that remove interstitial sodium when an element is inserted. Several sensors can communicate to the monitoring system using wavelength division multiplexing on a single fiber. There is not sufficient bandwidth to monitor twelve sensor assemblies in each fuel element, each measuring at several levels, in 54 fuel elements. Several trunks, but not a large

number, connect to the monitoring system. This is well-known technology used, for example, in under-sea cables.

I.1.5 Thermal analysis

A study of thermal properties of a fuel element began by varying the number of coolant tubes and their sizes, to provide a sufficiently large fuel paste volume fraction to produce a critical reactor. The investigation involved a series of experiments using the OpenMC (Monte Carlo) neutron-transport simulator [38] using data from ENDF/B-VIII.0 [9], balanced against maximizing the number of coolant tubes to increase overall thermal conductivity — subject of course to the ability to fabricate them. The conclusion was that 271 hexagonal coolant tubes, each with 3.125 mm interior edge-to-edge width (the estimated limit of fabrication ability) is the maximum number. An active region of 1500–1644 mm rather than the PRISM dimension of 1067 mm was also a result of this study.

The thermal analysis was conducted in two stages. Two dimensional analysis of an axial slice determined that with a linear coolant temperature gradient the axial fuel temperature gradient is locally linear. Using the linear temperature gradient approximation allowed to reduce the full three-dimensional heat equation to what is colloquially called a *2.5 dimensional* equation by eliminating the axial term in the Laplacian. Mathematical details are described in Appendix A.

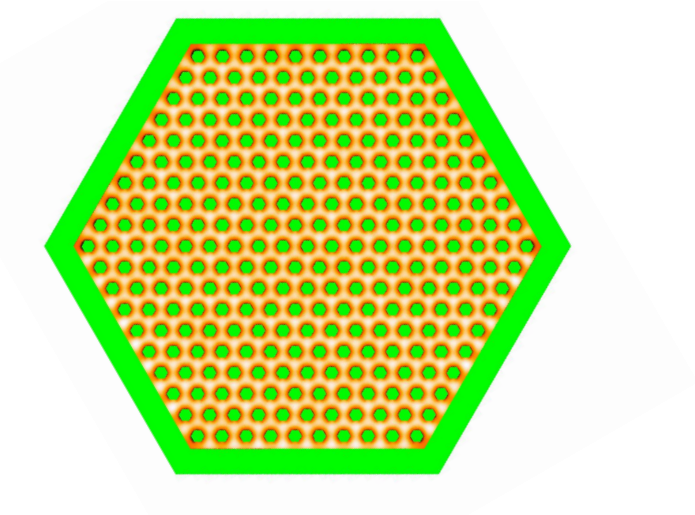

Figure I.3: Thermal solution in a fuel element with 271 coolant tubes

As will be described in Section I.3.1, fresh fuel is solid 50 µm particles. During irradiation porosity increases, allowing sodium to intrude, which increases conductivity. At about 2% burnup porosity stops increasing. Fission products continue to increase, which decreases conductivity. The results of eight calculations with $T_{\text{coolant}} = 775\,\text{K}$ are shown in Table I.3. One solution is illustrated in Figure I.3.

Table I.3: Thermal Study Results

		Temperature (K)		Conductivity
Burnup %	Porosity %	Max.	Avg.	$\text{W m}^{-1}\,\text{K}^{-1}$
0	0	955.9	914.9	42.96 - 44.44
1	12.5	942.9	905.9	44.97 - 45.71
2	25	930.6	896.5	47.07 - 47.14
3	25	930.8	896.5	47.06 - 47.12
4	25	930.5	896.5	47.04 - 47.10
5	25	930.3	896.5	47.03 - 47.09
6	25	929.9	896.5	47.01 - 47.07
7	25	931.3	896.4	47.00 - 47.06

The solutions for several coolant tube densities, all with the same paste area fraction of 0.6762 resulting from the 3.125 mm coolant tube width in the 271-tube case, but necessarily different structure and coolant fractions, with 5% burnup fuel (the equilibrium processing target), are shown in Table I.4.

Table I.4: Thermal Study Results with Several Tube Numbers

Number of Tubes		Temperature (K)			Tube Dimensions (mm)			Coolant
Per Edge	Total	Max.	Avg.	σ	Width	Spacing	Clearance	Fraction
10	271	930	896	22.97	3.125	8.787	3.793	0.1102
9	217	958	917	28.56	3.634	9.807	4.225	0.1193
8	169	997	944	36.05	4.277	11.09	4.767	0.1287
7	127	1052	983	47.37	5.119	12.76	5.462	0.1385
6	91	1134	1039	64.86	6.264	15.01	6.393	0.1486
5	61	1262	1129	94.26	7.703	18.23	7.703	0.1591
4	37	1501	1286	148.6	10.51	23.16	9.646	0.1700

Although the coolant fraction increases nearly linearly as the number of coolant tubes per edge decreases, temperatures nonetheless increase rapidly because the average distance of fuel from coolant increases: Coolant tube spacing increases quadratically, and the solution of the one-dimensional heat equation is quadratic.

Fuel in EBR-II operated at a maximum temperature of ≈ 1000 K. Lower radial temperature gradients give a correspondingly small low-power to full-power Doppler reactivity swing, resulting in reduced control reactivity requirements and less excess reactivity available for accidentral insertion [12, § IV.A.1].

I.1.6 Coolant Hydraulic Analysis

Hydraulic analysis requires ensuring that the temperatures of coolant emerging from the tops of coolant tubes are nearly equal to each other and nearly equal to the temperature of coolant emerging from the tops of areas, called jackets, around fuel elements. If this is not so, thermal striping occurs above the core. This required consideration of the *hydraulic diameters* of different coolant-flow regions, due to their different shapes. The hydraulic diameter affects cooling efficiency.

Table I.5: Hydraulic Study Results with Several Tube Numbers

Number of Tubes		η	τ	ΔP	Velocity (m/s)	
Per Edge	Total	(mm)	(mm)	(PSI)	Tubes	Jacket
10	271	3.1255	4.78	81.68	32.62	57.43
9	217	3.6338	5.32	58.90	30.14	51.41
8	169	4.2774	5.95	42.05	27.93	45.90
7	127	5.1185	6.69	29.55	25.95	40.75
6	91	6.2644	7.57	20.28	24.18	35.89
5	61	7.9170	8.68	13.43	22.59	31.24
4	37	10.506	10.13	8.403	21.14	26.65

Detailed description of the mathematical analysis method appears in Appendix B. The results for

several coolant tube densities are shown in Table I.5. η is coolant tube interior edge-to-edge width. τ is the outer coolant jacket thickness — half the spacing between elements.

I.1.7 Gas Management

Capillaries in three of the six corners are used for gas management. Those capillaries are protected from intruding sodium by the U-turns in the top plate, in the unlikely event that sodium sloshes 22 mm during a strong earthquake.

Fission gases that escape from fuel and then from sodium collect in the plenum above sodium. Fission gases that remain within fuel particle pores might be persuaded by the eductors to escape. Some fission gases that remain within solid regions of fuel particles might also be encouraged by vibration in eductors to find their way out through microcracks and grain boundaries.

Fission gases are swept out of the plenum by an argon diluent admitted through one (or two) of the gas capillaries, with gases removed at the other two (or one) of the gas capillaries. Sodium vapor is removed from gas lines by cold traps. If individual-element or sectoral return channels are provided, detailed isotopic analyses using gamma spectrometry are possible.

The diluent flow also regulates pressure within fuel elements.

If a static axial breeding blanket is added, the diluent would be injected at its bottom because its particles are not circulating. This bottom-up percolation ensures that fission gases, and fission products including caesium, iodine, and tellurium, and fines, are scavenged from within the fertile matrix and tend to migrate toward the top.

I.2 Grid Plate

The grid plate supports a hexagonal lattice of fuel, control, and shield elements, and motive sodium pumps. There are five concentric hexagonal rings, numbered 1–5 counting outward from the central position. There are $6n$ positions in ring n.

The central seat contains a wet control assembly that is cooled and lubricated by coolant sodium flow, connections for fission gas removal and pressure management, and connections for measurement instruments such as temperature, pressure, flow meters for the motive sodium, and temperature-compensated FBG strain gauges under each seat.

Ring 1 consists entirely of fuel elements. Ring 2 contains six wet control assemblies, one at each corner, and six fuel elements, one on each edge. The six corner control elements in ring 2 can change reactivity in a sector to accommodate removing fuel elements and the outer

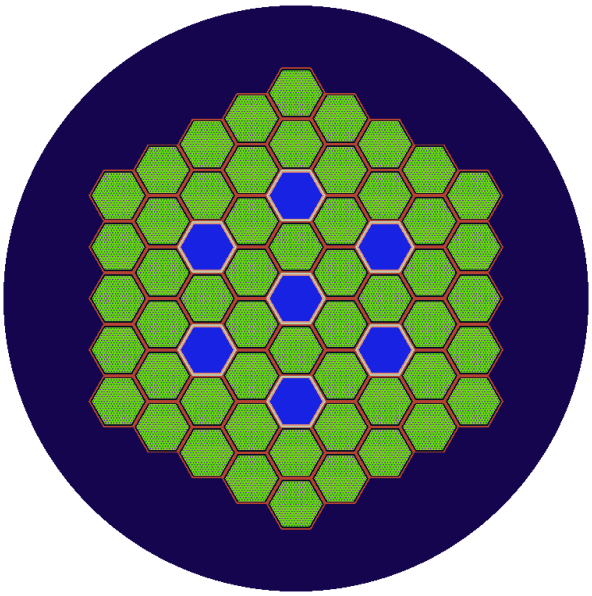

Figure I.4: Core Lattice

shield/reflector elements. Rings 3 and 4 contain 18 and 24 fuel elements, respectively, with 54 fuel elements overall. Ring 5 consists entirely of 30 shield/reflector elements, bringing the total number of positions to 91. The core lattice is illustrated in Figure I.4. The outer reflector is shown as solid instead of as a lattice of elements because computation using OpenMC was faster.

PRISM reactors include a neutron source in the central element, three control elements and three "ultimate shutdown" elements in ring 3, and six control elements in ring 6. This design is intentionally simplified, but only for purposes of exposition. A real design might incorporate a more robust system.

Fuel circulation is powered by six electromagnetic pumps in the grid plate, one along each edge, operating in series, with a small plenum having an inert gas head between each pair of pumps. Plenums smooth out pressure ripples and eliminate fluid hammer. The inert gas plenums are connected to the monitoring and control system. At the periphery, and between each pair of rings, there is a hexagonal ring of circulating sodium. Downstream of each pump there is a tangential inward bleed from the pump circuit to the outermost such ring, which has a tangential bleed outward to a venturi before each plenum, to complete the circuit. From each hexagonal circulation ring other than the innermost one, there is a tangential bleed to a ring around each element inwardly adjacent to the circulation ring. In the ring around each element there is a tangential bleed into the eductor at each corner. 120° downstream from injection into the circum-element ring there is a tangential bleed into the next inward circulation ring, resulting in flow being in the same direction in every circulation ring and every circum-element ring (flows in alternating directions would require two mirror-image sets of fuel elements). After the sixth eductor the circum-element ring is completed at a venturi into the outward circulation ring, which equalizes flow velocities throughout the circum-element ring and prevents the problem that would have been caused if the final eductor in a "dead-end" channel becomes blocked. Every curve in this circuit is a tractrix. The other flows in the grid plate are similarly organized.

Shield/reflector elements are filled with the same sort of W-15Cr-8Fe-5Hf sintered particle block as the neutron shield region in fuel elements.

With the exception of the control elements, seats in the grid plate are mechanically identical but different kinds of elements have different fluidic connections in the interface plug. Shield/reflector elements require no connection to motive sodium, fuel-processor fuel slurry flow, or gas management. Connections for the hydraulic channels to retract locking pins are entirely within each element.

The grid plate is fabricated as a multi-layer sandwich, with half-channels machined or etched into each layer. This is within the demonstrated capability of industrial HIP at smaller scales; scale-up to the dimensions required here is an engineering development task, not a fundamental barrier. Separate layers are needed for each flow, with vertical position assignments to be determined by final detailed thermal and hydraulic analysis. Because the walls of elements are separated from each other by a coolant-flow channel $\approx 9.5\,\text{mm}$ thick, and coolant must flow from below the grid plate through holes into those regions, circulation channels must be below, not between, the elements. So as not to require a three-dimensional fluid channel structure within the grid plate, channels proceed through the hydraulic-interface plug, with tangential bleeds to and venturies from tractrix elbows. When a fuel element is removed a dummy element is inserted to maintain circulation. Alternatively, the valves described in Section I.1.3 divert flows into parallel channels around the hydraulic interface socket. The channels contain:

- Motive sodium.

- Slurry flow to the fuel processor.
- Slurry flow from the fuel processor.
- Gas flow channel systems for fission gas and pressure management described in Section I.1.7

Below each element seat, coolant enters through a nozzle, with the sizes and shapes of nozzles selected to match differences in radial zone reactivity and heat production.

The grid plate is supported by a six-arm hexagonal radial structure of RAFM girders attached to the ridges of the six-bin hex hopper at the bottom of the vessel described in Section I.4.2. Sliding joints along each arm accommodate differential thermal expansion of the grid plate and vessel.

I.2.1 Optional Maintenance Seats

Six maintenance seat positions, one along each edge in an optional incomplete ring 6, could be included.

The maintenance seats have connections similar to fuel seats, but contain additional hydraulic valves that control whether the return-slurry path contains fuel or clean sodium, to allow elements to be emptied or filled. This allows inspection and servicing without complete shutdown. An alternative to hydraulically-activated valves to control emptying and filling is to use bucking EM pumps. These seats are probably redundant to the storage annulus described in Section I.7. An additional ring would add about 30 cm to the internal edge-to-edge width of the primary vessel.

I.3 Fuel

I.3.1 Fuel Morphology

Fuel in IMFR consists of a sodium paste of metallic particles having sizes that follow a log normal distribution with $\mu \approx 50\,\mu m$ and $\sigma \approx 0.75$. The random-close-packing volume mixing ratio with uniform size is $\approx 64\%$, but increases as σ increases [19, 37, 24, 43]. A small diameter is desired, subject to fabrication ability and hydraulic stability, but not so small as to be suspended in the "quiet zone" by Brownian motion ($\approx 3\,\mu m$). 50 µm is an estimated compromise. A log normal size distribution is a natural consequence of fabrication methods; a single size would require particle sorting. $\sigma \approx 0.75$, and therefore $\approx 78\%$ VMR paste, are estimates.

Because fuel in EBR-II was in continuous contact with cladding, plutonium formed eutectic compounds with iron, and lanthanide fission products formed both eutectic and brittle compounds with iron, eventually compromising fuel cladding [29]. With mobile fuel there is no prolonged intimate contact between fuel and structure. Chemical reactions between fuel and structure are effectively eliminated. Mobile fuel causes abrasion, but that is addressed by using RAFM instead of HT-9, 304, or 316L, and coating surfaces with W-10Ta.

Fuel slugs in EBR-II were fabricated with $\approx 75\%$ "smear density," that is, $\approx 85\%$ of the internal diameter of fuel pin cladding. Fission gases accumulated in closed pores, causing fuel to swell radially $\approx 18\%$ and axially $\approx 2\%$, corresponding to $\approx$ 35-40% volumetric increase. The rate abruptly decreased at $\approx 1.6\%$ burnup when pores became interconnected and opened to the surface. Thermal conductivity increased as interconnected porosity increased due to sodium intrusion [29, P. 95].

Fuel particles in IMFR will swell for the same reason. Pores will interconnect and open to the surface at lower burnup because diffusion paths are 1.4% as long, resulting in ≈5-9% radial increase. The final porosity will be ≈25-35%. These conjectures, extrapolated from EBR-II fuel behavior, require experimental verification. The thermal calculations reported in Section I.1.5 assumed 25% porosity. If porosity is greater operating temperatures will be lower because of increased thermal conductivity. See Table I.3 and Appendix E.

After the expansion rate abruptly decreased at 1.6% burnup, the diameter of EBR-II fuel slugs continued to expand due to accumulation of metallic fission products at the rate of 1.18% per percent of burnup [29, p. 98]. Thermal conductivity slowly decreased after the initial abrupt decrease due to reduced porosity and accumulation of fission products.

IMFR particles will expand at that rate. Pores will shrink as metal expands. It is conjectured, but needs to be verified, that pores will not begin to close until the solid fraction exceeds 92%, which does not occur until burnup exceeds ≈7%. When pores begin to close, gas generation forces them open again, so further gas-driven expansion does not occur. Particles' thermal conductivity does not decrease due to sodium expulsion but does decrease due to fission particle accumulation.

The fuel processing rate is targeted at average 5% burnup. At 1.6% burnup particles will expand to ≈55 µm due to gas accumulation. At 5% burnup particles will expand further to ≈58 µm due to fission product accumulation. This modest expansion will not cause clogging or bridging, and will not compromise circulation in fuel elements.

If the particle size distribution were to change, resulting in paste VMR changing, it is useful to consider changes in viscosity. Viscosity of a Newtonian slurry follows the Krieger-Dougherty relationship, *viz.*

$$\eta_r = \left(1 - \frac{\phi}{\phi_m}\right)^{-[\eta]\,\phi_m} \tag{I.1}$$

where η_r is the viscosity multiplier for the fluid (sodium), $\phi_m \approx 0.85$ is the "jamming" VMR, which causes the paste to behave as a rigid solid, and $[\eta]$ is the intrinsic viscosity, usually ≈ 2.5, the Einstein coefficient for spheres [33, 17, 18]. In the unlikely event that paste VMR increases from $\phi \approx 78\%$ to ≈80%, the viscosity multiplier η_r increases from ≈201 to ≈412. That is, paste viscosity roughly doubles. At ≈78% VMR fuel paste is a Bingham plastic. Pretending the paste is a Newtonian slurry is not physically realistic: The calculated viscosity at ≈78% would be the ridiculously small 43.5 mPa s. But the Krieger-Dougherty relationship is often used to approximate the viscosity *change* in Bingham plastics. High initial viscosity resists oscillations, and higher viscosity, if the particle size distribution changes due to particle swelling, resists oscillations more strongly, but does not impede fuel mobility until the VMR approaches the "jamming" limit.

Alloy migration was studied in EBR-II fuel pins. The effect is expected to be much smaller in 50 µm fuel particles. Detailed analysis appears in Appendix C.

When fuel particles expand due to fission product accumulation or increased temperature, fuel paste expands in the axial direction; there is no radial strain beyond the weight of fuel.

Fuel-cladding chemical interaction (FCCI) depends to some extent upon fuel alloy component migration. FCMI in EBR II was largely strain due to gas pressure and fuel slug expansion. Both were cited as major factors limiting duration of fuel pin residence in the reactor. Both are effectively eliminated in IMFR. Fuel elements should have forty year service life, limited by abrasion and

neutron damage — but this needs to be extrapolated from experiments, not estimated.

I.3.2 Fuel Alloy

Calculations using OpenMC [38] produced illustrative estimates of cold start and steady-state fuel alloy requirements at 475 K and 930 K. TRU (mostly plutonium) obtained from spent LWR fuel or reprocessed fast-reactor fuel, both fresh (i.e., without fission products) and after 5% burnup, were analyzed. The alloy weight percentages after simulations converged to $k_{\text{eff}} \approx 1.000$ and breeding ratio ≈ 1.00 are shown in Table I.6. The TRU requirements were different in the 475 K and 930 K calculations by less than 0.2%. The method to calculate the fast reactor TRU isotope mixture is described in Appendix D.1. The method to calculate alloy fractions is described in Appendix D.2.

Table I.6: Fuel Alloys

TRU Source	Alloy (930 K)	$\sigma_{k_{\text{eff}}}$	σ_{BR}
LWR	U–11.96Tr–6.1Zr	0.00070	0.0015
purified from fast reactors	U–10.8Tr–7.6Zr	0.00020	0.0005
after 5% burnup	U–11.1Tr–0.9Zr–5Fs	0.00042	0.0011

"Tr" is TRU and "Fs" is a fictitious element whimsically called "Fissium" as a collective term for the fission products shown in Table H.1. There are, of course, gradual transitions between these states. Because greater TRU is necessary as fuel changes during burnup, the breeding ratio must be slightly greater than 1.0 (e.g., using slightly less zirconium) until equilibrium is reached.

PRISM metallic-fuel designs use ≈20% TRU [49, Table II]. The lower TRU fractions obtained here, and the small difference in cold startup and steady-state requirements, result primarily from the increased fuel volume fraction made possible by the tube-in-paste geometry.

OpenMC is a snapshot; it cannot model temporal evolution of fuel alloy, neutron flux and spectra, and absorption cross sections. A more detailed analysis of neutron transport and fuel evolution would likely arrive at different, but probably not dramatically different, alloy compositions. The qualitative relationship between staring with LWR TRU as opposed to fast-reactor fissionables would remain. In a reactor started with TRU from fast reactors, a neutron source in the central element, as in PRISM, might not be necessary.

I.3.3 Breeding

The nominal goal is a 1.0 breeding ratio. This can be changed in several ways, mostly without structural changes:

- Move the shield/reflector elements outward and insert a ring of breeder elements. This would increase the diameter of the grid plate and primary vessel by ≈40 cm (a significant structural change).
- Change the fuel alloy, primarily by reducing zirconium to allow more U-238. Lower operating temperature allows lower amounts than would otherwise be required to increase solidus temperature.

- Replace shield/reflector elements in the outer ring with hybrid elements having half-fuel half-shield/reflector regions, in which fuel regions are filled with breeder particles instead of fuel particles. This would increase neutron flux outside the core, but probably not enough to compromise the targeted 100 year service of the primary vessel.
- Add axial snap-on cartridges. This would increase core reactivity by reflecting neutrons, and reduce neutron flux above the core. Depending upon their height, it might be possible to add them without increasing vessel height by allowing a reduced height of the open pool above the core.
- Change the control rod composition.
- Adjust coolant nozzles below the grid plate to increase temperature in breeding zones, which increases Doppler broadening of features in absorption spectra of ^{238}U.

In either "snap-on" breeder cartridges of breeder elements or half-breeder half-shield/reflector elements, the initial breeder particle load would be a $\approx 78\%$ paste of ^{238}U particles. Zirconium to increase the solidus temperature is probably not needed.

Continuous breeding in elements that have the same shape, grid plate interface, and nearly identical fluidic internals is possible. Instead of adding a ring to accommodate a radial breeding blanket, replace outer ring shield/reflector elements with hybrid elements, each one divided by a vertical wall, half filled with breeder particles and half filled with W-15Cr-8Fe-5Hf, in what would normally be part of the fuel region. The fuel half of this hybrid element would be filled with a $\approx 78\%$ paste of ^{238}U particles. Similarly to the bottom shield/reflector in fuel elements, the shield/reflector half would have a horizontal hafnium gradient.

A wall exactly dividing the element would need to bisect coolant tubes, incorporate them, or zig-zag around them. With 271 coolant tubes, a wall in the alley parallel to the diameter would allow slightly more (or less) than half to be breeder alloy. The dividing wall is bonded to the element by the HIP process that bonds the element.

With slightly more than half the capacity, and 2/3 the circulation rate (but the same per corner), the paste turnover rate within the breeder side of the element would be slightly faster than in a fuel element. It might be necessary to modulate the motive sodium flow rate to reduce this circulation, to bias breeding away from ^{239}Pu. Common motive sodium would be used. In either an additional-ring or hybrid-element case, a separate slurry channel would be required in the grid plate to return fuel from the processor, so as not to include fissionable isotopes in breeder elements.

There is a thermal imbalance, probably $\lesssim 10\,\mathrm{K}$, between the breeder and shield sides. The temperature difference could be reduced, but perhaps not eliminated, by incorporating baffles or calibrated nozzles at the bottom of the shield-side coolant tubes. If the divider bows, it would bow toward the solid shield because the breeder side would be hotter. This would not cause bridging or clogging.

The wall sections on the fuel side are identical to fuel elements. Two gas capillaries are connected on the breeder side for pressure maintenance and fission gas removal, as in fuel elements. On the shield side the gas capillary is used only for pressure regulation.

An axial breeding blanket that can be mechanically detached from a fuel element could be added. Breeding, and protection of the primary vessel, could be improved by adding a neutron shield above or as part of an axial breeding blanket. Like a neutron shield, it would not require slurry channels in the corners. Gas management would be similar to the fuel region, with argon injected at the bottom

as a scavenger, rather than at the top as a simple sweep. From the point of view of the reactor, material in snap-on breeder cartridges would be processed in batches rather than continuously, as continuous processing would increase the internal complexity of fuel elements by adding separate breeder fuel return channels. After moving a breeder cartridge to the fuel processor, its contents would be processed as a slurry at the same rate as breeder material from radial elements.

The axial cartridge interface is universal, allowing for the installation of snap-on breeder, reflector, or neutron shield boxes, including as axial "diagonal" breeding components above radial breeding elements (which could contribute 5-8% of total fissile production), depending on the desired core mission and local flux requirements.

I.4 Vessel Architecture and Primary Internals

I.4.1 Coolant Circulation

Primary and secondary coolant circulation are modeled on the PRISM design, preserving the pool-type reactor philosophy [49]. As in PRISM, $5.4\,\mathrm{m}^3\,\mathrm{s}^{-1}$ primary coolant flows upward from a high-pressure cold plenum below the core, through the core, and into the hot pool above the core.

To enhance modularity, conventional tube-and-shell heat exchangers are replaced with thin, flat, and broad printed-circuit heat exchangers (PCHE) mounted along the vessel walls [34]. Similarly, the four large electromagnetic (EM) pumps of PRISM are replaced by multiple modular EM pumps, also thin, flat, broad, and wall-mounted. The numbers and aspect ratios of these PCHE and EM pump units are optimized to facilitate extraction through maintenance ports while satisfying thermal, hydraulic, structural, and electromagnetic constraints.

Two arrangements should be considered in final design:

- Total-height Stripe Configuration: PCHEs and EM pumps are arranged as alternating vertical "stripes" along the vessel wall. This replicates the PRISM hydraulic path, including the U-turn in the pumps, though with a modular geometry.
- Integrated PCHE-above-EM Stripe Configuration: Each PCHE is mounted directly above its corresponding EM pump. This vertical alignment eliminates the need for complex internal U-turns or external ducting for the EM pump, reducing structural materials, simplifying the flow path, and simplifying the "redan" that separates the hot pool from the cold pool.

  Within this configuration, there are two possible relationships:

  - The PCHE and EM are physically separate units with an intervening cold "donut" that entirely surrounds the core.
  - The PCHE and EM are combined into a single physical unit or connected by a tapered nozzle.

The total-height stripe configuration maximizes the length of EM pumps, improving electromagnetic efficiency. The integrated PCHE-above-EM stripe configuration eliminates the bottom-to-top EM pump U-turn and the associated structural materials. The length of EM pumps can be increased by constructing two-stage tandem pumps, with the lower stage horizontal below the grid plate and connected to the upper stage by a donut, or a tapered nozzle and tractrix elbow. The

choice between these configurations depends upon detailed thermal, hydraulic, structural, and electromagnetic design considerations that are beyond the scope of this conceptual monograph.

In all configurations, as in PRISM, a structural partition (or *redan*) isolates the hot pool from the cold pool. This partition ensures that the only viable path for sodium circulation is through the PCHE-EM circuits, preventing a thermal-hydraulic short-circuit. The passive safety of the PRISM architecture is preserved: In the event of a total loss of forced flow, the vertical displacement between the core and the heat exchangers' inlets provides the buoyancy head necessary to sustain convective circulation.

I.4.2 Vessel Dimensions

The primary vessel is a hexagonal prism constructed from 65 mm thick RAFM steel, with a total vertical height of 12.4 m at the corners. Even though the vessel is not subject to abrasion, RAFM is used to provide thermal compatibility. Each corner includes additional structural elements to reinforce the hexagon's weakest regions against hydrostatic and seismic loads. This structure is positioned almost entirely below grade for seismic and radiological protection.

The edge-to-edge internal width is 7.5 m, or 8.7 m corner-to-corner.

As in PRISM, the upper 3 m of the reactor structure includes a double-rotating plug (DRP) assembly with a diameter matching the corner-to-corner diameter of the grid plate described in Section I.2 [49, Fig. 4]. This assembly provides the necessary 3 m of biological shielding. Nested large and small rotating plugs provide penetrations, mounted on the small rotating plug, to access any position within the core. The control systems are mounted on the rotating plug. All controls must be inserted, then their actuators disconnected, before the plug can be rotated. A significant difference is that in IMFR this system is rarely rotated because fuel elements are rarely physically moved.

Each PCHE-EM assembly is connected through, and can be removed through an individual dedicated port in the cover. If there is more than one PCHE-EM assembly along each edge they are connected by a manifold system above the cover. The total cross section provided by coaxial coolant tubes is $\approx 1.3\,\mathrm{m}^2$, allowing to transport $5.4\,\mathrm{m}^3\,\mathrm{s}^{-1}$ of secondary coolant at a velocity of $\approx 5\,\mathrm{m\,s}^{-1}$. With six PCHE-EM assemblies each connection would be a 750-800 mm diameter system. The diameters of coaxial assemblies are in inverse proportion to the number of PCHE-EM assemblies.

To avoid the complexity of connecting six pairs of coolant tubes, or six pairs of coolant tube manifolds, to the balance of plant on one side of the reactor, each of the six coolant systems is connected to an independent steam generator, one on each side of the reactor. This also provides gradual degradation of performance in the event of single-element failure. An arbitrarily large complex can be constructed using alternating rings of reactors and steam generators. Whether the steam generators are connected to more than one turbine will be determined by a detailed complete-plant design.

The top mounting flange extends further outward, with an overall corner-to-corner diameter of ≈ 10.9 m, to include the storage annulus described in Section I.7.

The internal volume is $\approx 600\,\mathrm{m}^3$ containing approximately $450\,\mathrm{m}^3$ of primary coolant sodium.

Similarly to the bottom of the fuel region in fuel elements, the vessel floor is also a six-bin hexagonal hopper with its apex at the center, consisting of six ridges, six valleys, and twelve facets. Facets are sloped 30° toward valleys that slope 26.6° from the center to vessel corners. There is a 200 mm hydraulic clearance below the core support grid.

To prevent accumulation of fines at the bottom of the vessel, there is a small ($< 0.5\%$) bleed from the central coolant-supply plenum directed downward toward the hexagonal hopper apex to sweep particles into the valleys and toward the corners. Each corner contains a channel that removes a very low-density slurry at $\approx 10\,\mathrm{mL\,min^{-1}}$ to an external hycrocyclone or diafilter for concentration. It is unlikely that eductors will be needed because of the high pressure in the cold pool.

I.4.3 Core Placement and Vertical Zonation

The reactor core is positioned within the center of the lower third of the vessel to leverage a massive sodium head for enhanced safety and hydraulic stability. The central volume of the vessel is divided into ten vertical zones.

At the base of the vessel, the below-core coolant plenum, resting on a support $\approx 200\,\mathrm{mm}$ above the apex of the bottom hopper to avoid a thermal "dead zone," receives primary coolant from the EM pumps. It is supported by vanes along each ridge of the hopper, which provide the strongest support.

Immediately above the plenum is the main support grid plate for the core described in Section I.2. Vertical zonation and component mapping are summarized in Table I.7.

Table I.7: IMFR Vertical Zonation

Component Zone	Z_{apex} **(m)**	**Engineering Rationale**
Top of Shield and Plug	+10.0	Worker-accessible surface; houses the double rotating plug (DRP) bearings and penetration headers.
Biological Shielding	+7.0 to +10.0	3.0 m of high-density shielding and DRP.
Cover Gas (Argon)	+5.5 to +7.0	1.5 m gap for aerosol mitigation and seismic sloshing clearance.
Open Hot Pool	+2.5 to +5.5	3.0 m of open sodium above assembly heads for flow redistribution to IHX inlets and thermal inertia.
Active Core Zone	+0.7 to +2.5	1.8 m high-flux region; contains the fuel element lattice.
Grid Plate / Plenum / Support Ribs	+0.2 to +0.7	0.5 m thick HIP-fused RAFM structure providing core support and flow distribution.
Bottom Clearance	+0.0 to +0.2	200 mm hydraulic sweep zone between rib bottoms and hopper surface.
Hopper Apex (Reference Datum)	0.0	Central reference origin for vessel floor geometry and hydraulic debris transport.
Vessel Floor / Valleys	-2.4 to 0.0	30° sloped facets guide fines and "crumbs" toward corner-integrated debris channels.

There are no penetrations through the vessel wall.

The hot pool establishes a 3-meter column of sodium, providing the significant thermal inertia required for walk-away passive safety.

The cover gas space is an inert argon buffer to accommodate thermal expansion and seismic sloshing.

I.5 Maintenance and Monitoring

Monitoring consists of continuous neutron and gamma radiation flux measurement, ultrasonic tomographic measurement of temperatures above the core, and periodic examination using the resident robot's integrated ultrasonic transducers to verify the integrity of individual elements' hexagonal ducts, coolant tubes, sodium levels, fuel paste levels, and the internal partitions in hybrid elements.

Although elements could be at least partly examined in place, examining all elements in an optional internal maintenance seat (Section I.2.1) or a seat in the storage annulus (Section I.7) allows to exploit their sixfold 60° geometric symmetry to rotate the element in the seat and examine it tomographically from six directions. Because the hot pool of sodium above fuel elements is thicker than their height, a fuel element can be lifted directly out of the core from any position and moved to a maintenance seat for inspection without disturbing any others.

Maintenance consists of replacing elements that periodic examination reveals to have damage or hazardous conditions such as stuck fuel or thinning walls or coolant tubes.

One (or more) of the six optional maintenance seats, or a special position, is equipped with an inductive coupler to charge a resident robot's sodium-sulfur battery.

I.6 External Connections

The core is connected to its environment through the cover, eliminating all penetrations through the wall. Power for sodium flowing in the external circuit is provided by electromagnetic pumps in the balance of plant.

There are three (or two) 1.5 mm^2 gas management tubes, and two or three 8 mm diameter connections to the fuel processor, two for slurry to and from fuel elements and (optionally) one for slurry returning to breeder elements.

These five (or six) fluid connections proceed downward from the center of the grid plate to the apex of the six-bin hopper, then along a ridge to a wall of the vessel, through tractrix elbows, where they rise to one coolant exit tube that is slightly larger than the others. If the fuel processor is distributed along edges outside the storage annulus, there would be several such connections.

This bundle exits from the hot-coolant tube into a separate transport system, wherein the bundle is surrounded by the following layers, from the innermost outward:

1. Outgoing high-temperature ($\approx$ 800 K) secondary coolant to prevent the inner lines from freezing and to provide process heat for the fuel processor.
2. Returning slightly-cooler ($\approx$ 785 K) secondary coolant, which is connected to a venturi in the tube that transports hot coolant to the balance of plant.
3. A vacuum Dewar jacket for convective and conductive insulation.
4. A jacket for radiative and further conductive insulation that serves the dual purposes of shielding the next layer from radiative heat transfer and allowing differential thermal expansion.
5. A jacket of W-15Cr-8Fe-5Hf particles, in gas instead of sodium to reduce thermal conductivity, for radiation protection.

6. A shell of 8 mm thick RAFM steel.

This coaxial system connects between the reactor, storage annulus, and fuel processor within a short subterranean tunnel having thick concrete walls and a 2 m thick ceiling of concrete and topsoil that provides environmental biological protection.

Circulation in the slurry tubes is powered by the motive sodium pumps in the grid plate. Circulation of secondary coolant to and from the fuel processor is powered by the secondary coolant pumps.

Power for the motive sodium pumps is provided by two conductors at opposite points of the grid plate that pass down to a ridge of the six-bin hopper, along the ridge to the vessel wall, then up opposite corners of the vessel. Using opposite corners avoids inducing eddy currents within coolant flow. A final design analysis might reasonably conclude that connections through all six corners are advantageous.

Corners are also used for connections to neutron and gamma detectors, ultrasonic transducers that provide continuous tomographic thermal mapping of the rising hot coolant, and other instruments.

I.7 Storage Annulus

An annular hexagonal ring about 0.5 meter thick and 4 m tall, filled with sodium (or NaK if active heating during shutdown is not desired), surrounds the primary vessel, with an air gap between the vessels. Chimneys for the reactor vessel auxiliary cooling system arise from the gap, to cool both vessels.

This storage annulus serves several functions:

- Storage for empty replacement elements to be used in the event that an active element within the reactor must be replaced.
- A buffer between the reactor and fuel processor. If the reactor is exactly full, elements in the storage annulus remain empty. If there is excess fuel in the system, it must go somewhere. The storage annulus eliminates storage within the fuel processor.
- If the reactor must be entirely defueled, sixty spare elements in the storage annulus provide more than enough storage volume.

This vessel's walls are 50 mm thick RAFM steel. The annulus contains storage seats for sixty fuel elements, but fewer might be emplaced. The seats are hydraulically active, similar to active seats within the reactor. The storage annulus is connected in series between the reactor and the fuel processor to allow short-lived fission products to decay. There are neutron barriers within the annulus between each pair of fuel element seats. Spacing of fuel elements, and the neutron barriers, prevent criticality even if every element is full.

Even with 54 fully-fueled fuel elements spaced uniformly around the annulus, passive air cooling is adequate.

Final design will determine whether the fuel processor occupies a distant hall, one edge outside the annulus, or surrounds it.

Pressure and fuel level measurements allow the total amount of fuel in the reactor to be adjusted. The relationship between the amounts of fuel in the storage annulus and the reactor is controlled by the relationship of eductor pressures in the storage annulus and active fuel elements. Fuel elements are fueled and defueled in place using these controls. The entire reactor can be fueled or de-fueled in less than 60 hours without physically moving any fuel element.

Reactor power can be controlled by changing the volume of fuel within the reactor. Whether this method, combined with the safety features described in Section I.8, can act sufficiently rapidly to eliminate the need for control assemblies is not addressed by this monograph.

I.8 Safety

I.8.1 Thermal Safety

There are two important thermal safety characteristics of all reactors.

As temperature increases structure expands. Reactivity is reduced because neutron economy is reduced by leakage.

As temperature increases the random motion of nuclei increases, causing the spectral features of neutron resonance absorption cross sections to broaden due to the Doppler effect. This is especially important in U-238 because it increases the probability of non-fission neutron capture, providing an immediate inherent negative reactivity feedback that suppresses the fission chain reaction. The *Doppler margin* — the effective reactivity suppression potential — is limited by thermal integrity; specifically, the temperature at which fuel melts, structural damage occurs, or coolant boils.

Reactivity, and the *worth* of reactivity, are expressed as

$$\rho = \frac{k_{\text{eff}} - 1}{k_{\text{eff}}} \text{ and } \rho(\$) = \frac{\rho}{\beta_{\text{eff}}}\,, \tag{I.2}$$

where k_{eff} is the effective multiplication factor, computed from the eigenvalues of the core, and β_{eff} is the effective delayed neutron fraction.

In EBR-II, in the event of loss of coolant flow, loss of heat sink, or unexpected increase in reactivity, the grid plate expanded horizontally, separating fuel assemblies and increasing neutron leakage, which reduced reactivity. This negative thermal reactivity worth due to radial expansion and sodium void was estimated to be in the range $\rho(\$) = -.54\,¢\,\text{K}^{-1}$ to $-.75\,¢\,\text{K}^{-1}$. Doppler broadening was reported in the range $\rho(\$) = -0.29\,¢\,\text{K}^{-1}$ to $-1.0\,¢\,\text{K}^{-1}$ [50, Tables IV-V] [20].

These effects, taken together with the enormous heat capacity of a sodium-cooled pool-type design, provided passive "walk-away" safety, with fuel pin cladding returning to normal operating temperatures within seven minutes after loss of coolant flow or loss of heat sink, as demonstrated to an invited international audience in 1986 [5] [39, p. 117-118].

The effect of structural expansion was not calculated for IMFR but is expected to be in the same range. For IMFR, k_{eff} and β_{eff} were calculated by OpenMC using 20,000 points per batch, 500 inactive batches, and 1000 batches overall. The effect of Doppler broadening was calculated by increasing temperature up to 200 K above the nominal peak operating temperature of ≈ 930 K. The calculated Doppler worth was $\rho(\$) = -0.51¢\,\text{K}^{-1}$. Because IMFR operates at a temperature about 60 K below EBR-II, IMFR has about 30 ¢ greater Doppler margin.

An important additional phenomenon in IMFR is that fuel elements contain a mobile paste. The paste cannot expand laterally because it already occupies the entire horizontal extent of the fuel element. Instead, and more importantly, the paste expands axially and rapidly as temperature increases; solid metal expansion is much slower. Expansion reduces neutron economy by two effects: Reducing density and increasing axial extent, which increases surface area and neutron leakage.

Using the fast reactor fuel alloy in Table I.6, k_{eff} and β_{eff} were calculated to assess worth as a function of density and expansion without changing the fuel temperature, that is, Doppler sensitivity was not included. The method is explained in Appendix F. The results were

$$\begin{aligned} \frac{\partial \rho(\$)}{\partial H} &\approx -5.56\,¢\,\text{mm}^{-1} \text{ and} \\ \frac{\partial H}{\partial T} &\approx 0.13\ \text{mm}\,K^{-1} \\ \frac{\partial \rho(\$)}{\partial T} = \frac{\partial \rho(\$)}{\partial H}\,\frac{\partial H}{\partial T} &\approx -0.73\,¢\,K^{-1}\,, \end{aligned} \tag{I.3}$$

In the event of loss of coolant flow or heat sink, fuel paste temperature increases, density decreases, and it expands vertically into the gas plenums above the fuel regions of fuel elements. For fuel to expand 22 mm, completely consuming the plenum, it would be necessary to increase the temperature by 169 K to 1099 K, well below the 1154 K boiling point of sodium. In extremis, before fuel reaches the sodium boiling point, it can expand 7.2 mm into the "quiet zone," which would force sodium into the gas management system.

In solid-fuel reactors, boiling increases reactivity, but with mobile paste it decreases reactivity by decreasing fuel density. The SUPO homogeneous-fuel reactor (a boiling aqueous solution of uranyl nitrate) demonstrated remarkable stability [35] [3, pp. 133ff]. Analysis of a boiling-sodium homogeneous-fuel reactor by the present author [45] using the method of Stein and Kasten [46] also showed remarkable stability, and suggests that similar stability is to be expected in IMFR, without the high-frequency "hiccups" observed in low-viscosity homogeneous-fuel reactors. The worth of boiling paste has not been quantified. Whether it is larger or smaller than the worth of expansion of Bingham plastic fuel — or perhaps positive, a hazard— is a subject for future investigation.

Table I.8: Change in Reactivity Worth from ≈930 K to 1154 K

Reason	Rate	Amount
Structural expansion (224 K)	-0.45 ¢/K to -0.66 ¢/K	-$1.01 to -$1.48
Axial fuel expansion of 22 mm (169 K)	-0.749 ¢/K	-$1.26
Axial fuel expansion of 7.2 mm (55 K)	-0.749 ¢/K	-$0.42
Doppler margin (224 K)	-0.512 ¢/K	-$1.15
Total after 224 K increase		-$3.84 to -$4.31

The IMFR system achieves autonomous passive "walk-away" safety because, as in EBR-II, the grid plate expands as temperature increases, separating fuel elements and reducing neutron economy. As in EBR-II, the IMFR system is a sodium-cooled pool-type reactor. Because the IMFR structural form is modeled upon PRISM, which is modeled upon EBR-II, negative thermal structural reactivity worth due to structural expansion should be expected to be approximately the same.

Change in reactivity worth from the nominal peak operating temperature $\approx 930\,\mathrm{K}$ to the sodium boiling temperature of $1154\,\mathrm{K}$ is summarized in Table I.8. The contribution of the "axial" column in Table V in [50] is excluded from the first row because it is independently calculated here — but only for fuel, not for structure.

The IMFR demonstrates a unique coupling between fuel rheology and neutronic stability. Expansion is driven by internal power generation, which easily overcomes gravity. In an over-cooling transient, the temperature coefficient of reactivity is modulated by the effective viscosity of the $\approx 78\%$ paste, and is limited to contraction gravity can cause. While thermal contraction increases fissile density, fuel paste viscosity provides a significant damping term that prevents rapid compaction. Although there are no data at this time concerning the viscosity of a $\approx 78\%$ Bingham plastic of actinide particles in sodium, viscosity is expected to be much larger than would be computed by the Krieger-Dougherty equation, which is only applicable to Newtonian fluids. Large rheological impedance prevents the formation of power oscillations or damps them quickly, and is expected to ensure that the reactor maintains a stable power level without the high-frequency "chugging" or "hiccups" characteristic of less viscous mobile-fuel systems.

Residual decay heat is managed during shutdown by a passive Reactor Vessel Auxiliary Cooling System (RVACS), similar to the GE Vernova PRISM system [49]. This system utilizes natural air convection between the exterior of the primary vessel and the interior of the storage annulus to dissipate heat to the atmosphere. Given the high thermal conductivity of liquid sodium and the ≈ 400 tonne inventory of the primary pool, the IMFR remains thermally stable indefinitely without the requirement for active pumping or operator intervention. Fission is not proceeding in the storage annulus. This convection is sufficient to remove decay heat from both the reactor and storage annulus.

I.8.2 Seismic Response

The seismic design of the primary vessel must account for the hydrodynamic loads imposed by the large liquid sodium inventory. The system is intended to withstand an earthquake through a combination of base isolation and internal damping. Because a specific Design-Basis Earthquake (DBE) standard has not yet been defined for this conceptual description, this analysis attempts only to establish a sufficient seismic margin.

I.8.2.1 Base Isolation and RVACS Protection

As in PRISM, the entire reactor vessel, storage annulus, and fuel processor are mounted on lead-rubber bearings, which shift the fundamental frequency of the structure to $\approx 0.5\,\mathrm{Hz}$, filtering out high-frequency seismic energy. This isolation ensures that the Reactor Vessel Auxiliary Cooling System (RVACS) remains functional following a major event.

I.8.2.2 Resonant Frequency of Fuel Elements

The fundamental resonant frequencies of single elements, rigidly connected to the grid plate, were calculated by the Rayleigh-Ritz method. Approximations for fuel viscosity and inter-element coolant viscosity were applied. Forces and maximum deflections were calculated. The results are shown in Table I.9. Details of the calculation are shown in Appendix G.

Table I.9: Seismic Analysis Results

Element Type:	Fuel element		Shield element		Control element	
Resonant Frequency (hz)	82.1		115.4		43.7	
Damped Frequency (hz)	81.6		114.6		Overdamped	
Seismic Accelerations (g)	0.3	0.5	0.3	0.5	0.3	0.5
Forces on Elements (N)	83.373	138.96	1224.1	2040.2	184.22	307.04
Peak displacement (gap %)	1.86	3.10	1.72	2.87	Overdamped	
Mean displacement (gap %)	0.389	0.744	0.421	0.751	0.884	0.869

Resonant frequencies are all well above the 0.5-30 Hz frequency of most earthquake motions. The 30 Hz upper limit is recommended for high-frequency analysis of modular reactor designs [30]. Control elements do not vibrate because they are overdamped. Because different kinds of elements have different resonant frequencies, the core as a whole has a multi-modal resonance and should not be excited into coherent resonance by high-frequency seismic motions that are not damped by the vessel's lead-rubber bearings, even if the vessel "bottoms out" through them. A total-core frequency analysis as part of detailed design is expected to confirm this.

Sloshing and Hydrodynamic Response are expected to be the same as in a similar PRISM design.

If a catastrophe were to damage fuel elements, allowing fuel paste to escape, the six-bin hexagonal hopper at the bottom of the main vessel serves a critical safety function to spread the fuel radially and separate it into non-interacting regions. It is unlikely that all fuel elements would rupture. Even if so, the six fractions of fuel would each be in a region $< 45\%$ the thickness of the core with surface-to-volume ratio more than three times larger, and widely separated, giving $k_{\text{eff}} \ll 1$. Even if pockets of criticality remain, the enormous mass of coolant sodium and $\approx 22\%$ sodium in fuel, and the very high 1154 K boiling temperature of sodium, provide a large safety margin. The worst-case result of any catastrophic damage would be an expensive mess rather than a radiological hazard to safety or health.

I.8.2.3 Fuel Bed Stability

In civil engineering, seismic-induced liquefaction is a structural hazard. In IMFR it functions as an inherent passive negative reactivity feedback mechanism: Any seismic-induced fluidization reduces fuel density.

This transition from the usual $\approx 78\%$ state to a fluidized, lower-density state, if it occurs, increases neutron leakage, effectively providing a passive, rapid shutdown mechanism during seismic acceleration. Internal motion is inhibited by Bingham plastic viscosity until the seismic-induced shear stress exceeds the paste's yield stress. Once the acceleration subsides, the fuel settles back into its packed configuration. Although viscosity increases as fuel density increases, there is the possibility that fuel returning to its pre-seismic state will overshoot, resulting in density greater than $\approx 78\%$, and concomitant increase in reactivity and temperature. As explained in Section I.8.1, this quickly results in rapid thermal, not seismic expansion, and reduced reactivity. Because of the high viscosity of a Bingham plastic, oscillations are unlikely, and divergent oscillations are impossible.

Rather than a threat to stability, fuel bed fluidization acts as a passive, autonomous "seismic trip" that enhances the IMFR's inherent safety profile. If the yield stress is not exceeded, the paste remains in its packed configuration and the reactor behaves as a fixed-fuel system with respect to

seismic response — still safe, just without this particular passive feedback mechanism.

Part II

Fuel Processing

The first plan for this project was pyroprocess electrolytic refining, as had been done at EBR-II [48], where a stainless steel anode basket held fuel slugs. A basket cannot be used in a continuous system intended to have no moving parts, so liquid metal electrodes were investigated.

When fuel is dissolved in cadmium, several intermetallic compounds form with cadmium or between fission products. Their solubilities depend upon temperature. At a temperature very close to cadmium's melting point only indium, palladium, and uranium remain in solution.

Several intermetallic compounds have low density and do not dissolve. They produce a floating insulating layer that significantly reduces anode efficiency; it seemed that an undesirable mechanical anode would be necessary.

Instead of a pyroprocessor using a moving mechanical anode, a very small continuous autonomous reflux thermochemical system was developed. It separates fission products in a continuous-flow counter-current multi-stage fractional crystallization cascade, rather than a pyroprocessor. One stage is illustrated in Figure II.1. Specification of dimensions is beyond the scope of this conceptual study.

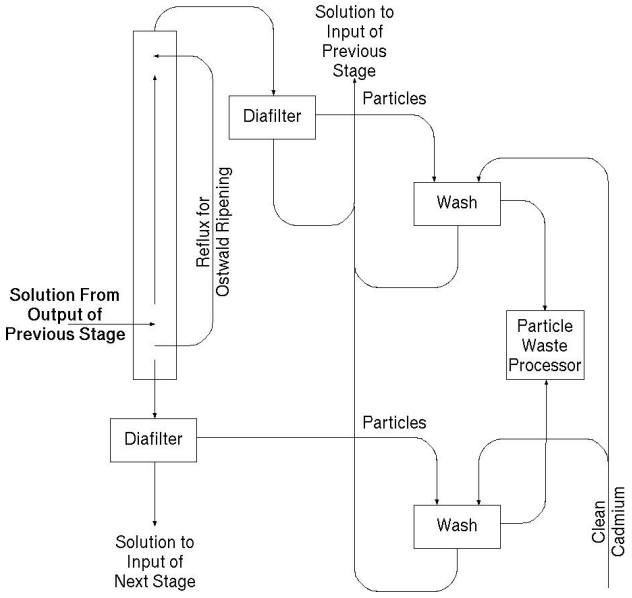

Figure II.1: One Stage of Fuel Processor

Although this methodology is adapted from established industrial practices in high-purity metal refining, and the chemistry was investigated by Argonne and Idaho National Laboratories [31, 4], significant investigation is required to determine feasibility of this concept, particularly regarding long-term materials compatibility, irradiation effects, criticality safety under continuous operation, and process control in a radioactive environment. The combination of methods described here has not previously been described.

Cadmium was selected rather than indium-bismuth because intermetallic compounds that form with it can be dissociated at moderate temperatures and exhibit useful solubility differences.

Even if the entire process is not feasible, the initial dissolution step that removes noble metals, several intermetallic compounds, and volatile fission products is a useful precursor to a pyroprocessor by eliminating the floating insulating layer on the anode. Equally importantly, volatile alkali metals, which are very difficult to remove from electrolyte, do not enter the pyroprocessor.

A summary of the intermetallic compounds and their separation behaviors is shown in Table II.1.

Table II.1: Fast Reactor Fission Products and Primary Separation Behavior

Element Group	Primary Fate
Noble metals (Mo, Tc, Ru, Rh, Pd + Zr compounds)	Sink in 1000 K stage
Lanthanides (Ce, Eu, Nd, etc.)	Float/sink in 775 K stages
Alkali/alkaline earth (Cs, Rb, Ba, Sr)	Vapor or float (halides)
Halides (I, Br)	Float as Ba compounds
Gases (Kr, Xe)	Off-gas
Others (Ag, In, etc.)	Stage-dependent

High-temperature high-velocity sodium vapor produced by a flash evaporator that cools the shell of the 1450–1550 K fuel alloy induction furnace provides high-temperature process heat. Process heat at lower temperatures is provided by the 800 K secondary coolant that is also used to keep the transfer lines from freezing.

The 840 MWth reactor consumes ≈ 310 kg of fuel — almost exclusively plutonium and other TRU — per year, $\approx 0.84\,\mathrm{kg\,d^{-1}}$. To simplify discussion, assume one kilogram per day. Processing ≈ 20 kg of fuel per day ($\approx 14\,\mathrm{g\,min^{-1}}$ of fuel particles), results in an equilibrium average 5% burnup. Fresh fuel particles have a density of $\approx 17\,\mathrm{g\,cm^{-3}}$ and 1.6% burnup fuel particles have a density of $10.4\,\mathrm{g\,cm^{-3}}$ (which doesn't change much after 1.6% burnup). Assuming average particle burnup >1.6%, it is necessary to process $\approx 2.4\,\mathrm{L\,d^{-1}}$ of fuel, $\approx 31\,\mathrm{L\,d^{-1}}$ of $\approx 7.8\%$ slurry, or $\approx 21\,\mathrm{cm^3\,min^{-1}}$ of slurry containing $\approx 1.6\,\mathrm{cm^3\,min^{-1}}$ of fuel particles.

Fuel processing proceeds through the following stages:

1. Separate fuel particles from sodium.
2. Dissolve fuel particles in cadmium.
3. Separate fission products from unused fuel.
4. Create final fission product waste forms.
5. Reconstitute fuel using purified unused fuel and additional ^{238}U.

The following sections outline each stage. Details of the processes are described in Appendix H.

II.1 Separating Fuel Particles from Sodium

When the $240\,\mathrm{L\,h^{-1}}$, $4\,\mathrm{L\,min^{-1}}$, of $\approx 7.8\%$ slurry arrives at the processor, a $21\,\mathrm{cm^3\,min^{-1}}$ $\approx 7.8\%$ slurry is diverted for processing. An aerosol is formed using a 1250 K sodium-vapor nebulizer with a flow rate of 12–15 liters per minute. This vaporizes the 92.2% carrier sodium and its dissolved fission products, especially caesium and rubidium. The remaining incoming slurry is returned to the reactor, with new fuel added at the rate of $\approx 14\,\mathrm{g\,min^{-1}}$.

Fuel particles are separated from sodium vapor in a cyclone separator, with the overflow going to the fractionation tower described in Section II.2. Further sodium is removed by a cascade of hot argon cyclone separators. The argon and sodium overflow proceeds to the fractionation tower.

Fines that proceed with the overflow, including dissolved fission products such as strontium and barium that have boiling points above 1250 K, fall into the dissolver stage below the reflux fractionation tower. The underflow of argon and particles is sparged into the dissolver stage at mid level to produce a vortex.

II.2 Dissolving Fuel Particles

The dissolver stage serves several simultaneous functions. When fuel dissolves in molten cadmium at 1000 K, fission gases are released, volatile fission products (and some sodium) evaporate, noble metals precipitate, and insoluble intermetallic compounds crystallize. The extent of each process depends upon residence time. The required volume of the cadmium solvent is thus determined by the input flow rate, the target residence time, and the solubility limits of the fuel constituents.

Hydrocyclone performance — including residence time, separation efficiency, and criticality — is intrinsically coupled to the aspect ratio. A high-aspect-ratio "pencil" geometry is employed here to enhance separation efficiency and increase the surface-to-volume ratio, thereby providing passive criticality safety by maximizing neutron leakage.

Subsequent stages are also pencils. If their volume is sufficiently large to cause criticality hazards, the entire system can consist of several identical small modular systems operating in parallel. These might be arranged in an entirely separate processing hall, or as independent units, one along each edge outside the storage annulus.

The vapor overflow from the hycrocyclone enters the fractionation tower described in Appendix H.1.

The underflow from the hycrocyclone contains insoluble noble metals and insoluble intermetallic compounds shown in Table H.2.

Incoming fuel slurry contains sodium intermetallic compounds and halide salts, but sodium will be displaced from them by zirconium, barium, or strontium when fuel is dissolved. The resulting salts and intermetallic compounds are not soluble in cadmium at 1000 K. These and other intermetallic compounds are shown in Table H.3.

The argon sparge creates bubbles that move toward the center of the vortex, carrying light particles with them. The particles are removed from the vortex by a weir at the top of the cadmium hydrocyclone, then concentrated, washed, and cadmium is separated as described in Appendix H.1.

Caesium, rubidium, cadmium, and a very small amount of sodium escape as vapors. The difficulty of sodium to escape is one reason it was separated earlier. The other reason is that excess sodium might prematurely precipitate palladium-sodium intermetallic compounds. The number of argon cyclones, perhaps zero, depends upon whether sodium interferes in intermediate stages, and can be efficiently removed at the final stage. Volatile metal vapors are separately condensed in a reflux fractionation tower that returns cadmium and fines to the fuel dissolver. Caesium and rubidium proceed to the waste processor described in Section II.5, perhaps as vapors. Volatile metals' boiling points and saturation pressures are shown in Table II.2.

Table II.2: Volatile Metals' Boiling Points

Metal	Boiling Point (K)	P_{sat} at 1000 K	Destination
Sodium	1154	0.02 atm	Fuel slurry and other uses
Cadmium	1040	0.32 atm	Fuel dissolver
Rubidium	961	1.40 atm	High-level waste preparation
Caesium	944	1.85 atm	High-level waste preparation

The desired solute concentration is maintained by controlling the rate at which the solution is withdrawn through the underflow diafilter.

II.3 Separating Fission Products from Unused Fuel

The cadmium solution is pumped by electromagnet pumps through a series of counter-current multi-phase separation "pencil" columns illustrated in Figure II.1, wherein different intermetallic compounds crystallize and are removed at different temperatures. Fission products are removed in each stage, leaving actinides in solution in the last stage. The columns simultaneously partition dense and buoyant waste phases from the actinide-bearing carrier. Particles formed in each stage are removed using diafilters and washed in continuous-flow counter-current columns using clean cadmium, with permeate returning to the previous stage as shown in Figure II.1.

A summary of the partitioning stages is shown in Table II.3.

Table II.3: Partitioning by Processor Stage

Stage	Temp (K)	Primary Removed Species / Form
Dissolver / Hydrocyclone	1000	Noble metals, insolubles (sink); volatiles (vapor)
800 K stage	800	Ba, Sr, Y compounds (float/suspension)
775 K stage	775	Lanthanides (float/sink)
765 K stage	765	TRU compounds (sink)
600 K / Final	600	U, Pd, In polishing

The temperature of the penultimate stage is 775 K, and actinide solubility in that stage is still quite high. The input rate, solubility limits, recirculation rates, withdrawal rate, and criticality constraints determine the system stage-to-stage flow rate and the volume of each stage.

Each fractional-crystallization stage operates at a carefully-controlled temperature less than the previous stage. Each column is a "pencil," to eliminate the possibility of criticality. The cadmium solution from the previous stage is injected into each stage near the bottom. Fission products not removed in previous stages sequentially crystallize into cadmium-rich intermetallic compound particles in later stages, allowing stage-wise separation from the cadmium solvent. Low-density particles are harvested from the top by a diafilter, with part of the permeate and fines not removed by the filter proceeding to the previous stage, and part being refluxed within the stage, from below the inlet back to the top. High density particles are harvested by a diafilter below the inlet, with permeate proceeding to the next stage. The reflux rate determines the duration of Ostwald ripening, to convert colloidal suspensions and fines into more macroscopic particles. The definitions of "light" and "heavy" particles depend upon the upward cadmium flow velocity.

Particles removed by diafilters are washed with clean cadmium in continuous-flow counter-current columns, with reflux going to the previous stage, and then removed by another diafilter. Cadmium is removed from the concentrated and washed particles by a 900 K argon nebulizer. Because the columns are necessarily tall to contain sufficient volume, solutions are circulated by electromagnetic pumps instead of gravity.

Details of the separations in each stage are described in Section H.2.

In the solution remaining at the final stage, cadmium is removed and dissociated from uranium using a 1200 K argon nebulizer that also removes sodium introduced to remove palladium, and any that remains as a result of barium and zirconium having displaced it from sodium intermetallics, and not having evaporated from the 1000 K cadmium fuel dissolver. Indium will remain adhered to the uranium. In the 840 MWth reactor, indium accumulates at the rate of 22 grams per year. Indium, trace impurities, and magnesium that results from neutron absorption in sodium would have no effect on the neutronic, chemical, or mechanical properties of fuel, remaining below $\approx$200 ppm at the end of the system's 100 year service.

At every stage other than the palladium and final uranium separation stages, cadmium vapor and argon are sparged back into the cadmium fuel dissolver to maintain the vortex. In the palladium and uranium stages, argon, cadmium, and sodium vapors return to the fractionation tower so as not to add sodium to the cadmium fuel dissolver stage.

Uranium, transuranic, and zirconium powders are transported to the fuel reconstitution stage by eductors powered by argon or sodium vapor. Excess transuranics are used to start another fast-neutron breeder reactor, or to increase the TRU content in fuel during the transition to equilibrium 5% burnup, if the breeding ratio is greater than 1.0.

The separations need not be perfect, except that if palladium is contaminated with other materials it becomes radioactive waste rather than a potential profit center. The fuel phase need only be sufficiently pure that insignificant neutron poisons remain, and fuel can be reconstituted with the correct composition and physical properties. The waste phases are intended to contain actinides below the parts-per-million range.

Cooling for low-temperature phases is supplied by secondary sodium coolant returning from the balance of plant.

The author asked Dr. Yoon Il Chang, Associate Laboratory Director for Engineering Research at Argonne National Laboratory and technical architect and principal developer of the IFR program in the 1980s and 1990s, why the cadmium cathode in the EBR-II pyroprocessor was abandoned. He replied that cadmium vapor had "gotten into everything" in the processing hall, forcing substitution of an iron cathode. All phases described here are sealed, with an argon sweep returning cadmium vapor to the fractionation tower.

II.4 Alternative Lanthanide-Actinide processing

If separating lanthanide intermetallics from cadmium does not sufficiently accurately separate actinides from lanthanides, that is, the actinide carry over is more than the desired $\approx$1 ppm, one of several additional processes would be necessary. The most likely failure is in the 775 K stage, wherein when lanthanide-cadmium intermetallic compound crystals form, actinide-cadmium intermetallic compounds might form with them.

Several methods are possible. All would use very small processors, and would contain very low actinide concentrations. Criticality is not a concern so a single processor, not a separate processor per module, is possible.

One method is to reprocess precipitates by re-dissolving them and then processing them in a similar but much smaller and much shorter "polishing" processor.

Another method is to re-dissolve the precipitates in cadmium and use the solution as an anode in a pyroprocessor. This has several advantages compared to using a pyroprocessor alone: Insulating intermetallic compounds that would significantly reduce anode efficiency, and alkali metals that would be very difficult to separate from electrolyte, have been removed at earlier stages. Actinides would be reduced in a cadmium cathode, while lanthanides would remain in solution in the electrolyte, from which they can easily be removed by dissolving in water and adding ammonium phosphate. Resulting ammonium chloride can be removed from electrolyte by heating.

The preferred method is to form lanthanide and actinide chloride precipitates in liquid cadmium by sparging chlorine gas in a reflux column. As shown in Table II.4, they are significantly less dense than cadmium, and can easily be removed from the column. $CdCl_2$ is also inevitably formed, but the production rate can be reduced by careful temperature control.

Table II.4: Chloride Phase Separations and Density Partitioning at 775 K

Chloride Species	**Physical Form**	**Density** ($g\,cm^{-3}$)	
		Chloride	**Element**
Cd	Solvent	7.80	7.80
$LaCl_3$	Frozen Float	3.84	6.16
$CeCl_3$	Frozen Float	3.97	6.77
$PrCl_3$	Frozen Float	4.02	6.77
$NdCl_3$	Frozen Float	4.13	7.01
$PmCl_3$	Frozen Float	4.19	7.26
$SmCl_3$	Frozen Float	4.46	7.52
$EuCl_3$	Frozen Float	4.61	5.24
$GdCl_3$	Frozen Float	4.52	7.90
$DyCl_3$	Frozen Float	4.41	8.55
$CdCl_2$	Frozen Float	4.05	—
$MgCl_2$	Frozen Float	2.32	1.74
UCl_3	Frozen Float	5.50	19.05
$NpCl_3$	Frozen Float	5.58	20.25
$PuCl_3$	Frozen Float	5.70	19.84
$AmCl_3$	Frozen Float	5.87	13.67
$CmCl_3$	Frozen Float	5.87	13.51

The $CdCl_2$, $LnCl_3$, and $AnCl_3$ salts in cadmium overflow from the column to an intermediate molten Li-Cd carrier solvent reflux column that contains enough lithium metal to reduce $CdCl_2$ and $AnCl_3$. The resulting $LnCl_3$ and LiCl crystals are removed from the overflow. The process can be monitored and lithium addition controlled using electrochemical potentiometry or laser-induced breakdown spectroscopy of the solvent to detect excess lanthanides in solution, and cyclic voltammetry or optical absorption spectroscopy of the salt overflow to verify no actinide or cadmium chlorides remain.

$LnCl_3$ and LiCl are separated by volatilizing LiCl using a hot argon nebulizer. Argon and LiCl vapor are sparged into the electrolyte of an electrowinning cell that reduces LiCl into a cadmium cathode, closing one loop. Evolved chlorine is returned to the previous step, closing the other loop. This is the only electrochemical process, and its only purpose is to reduce LiCl to lithium for use in the previous step.

This method does not include a three-way density separation. Reducing $AnCl_3$ using lithium, and then reducing LiCl by electrowinning, is generally considered to be simpler than reducing $AnCl_3$ directly by electrowinning, not least because only one cathode regime is needed, not separate regimes for uranium and other actinides.

Lanthanide chlorides are dissolved in water, then converted to phosphates using ammonium phosphate. Lanthanide orthophosphate ($LnPO_4$) is the lanthanide equivalent of monazite, a very stable mineral.

Actinides are separated from cadmium by a hot argon nebulizer.

II.5 Waste Disposal

Barium, strontium, halide salts, and yttrium are removed together from the 800 K cadmium melt, and form a mixed powder aerosol stream when cadmium is removed by a hot argon nebulizer. This stream is combined with caesium and rubidium vapors from the cadmium dissolver (or liquids from the fractionation tower), and steam, in a mixing tube, where barium, caesium, rubidium, strontium, and yttrium form hydroxides and hydrogen. The aerosol of hydroxides and halides is sparged into a buffered pH-controlled aqueous slurry of alumina and silica, creating a hydrothermal synthesis to produce pollucite, rubicline, slawsonite/strontium-anorthite, celsian, bromo-sodalite, iodo-sodalite, yttrium aluminum garnet, and yttrium metasilicate, by the following reactions:

$$2Y(OH)_3 + 3SiO_2 \rightarrow Y_2Si_3O_9 + 3H_2O$$
$$3Y(OH)_3 + 2.5Al_2O_3 \rightarrow Y_3Al_5O_{12} + 4.5H_2O$$
$$CsOH + 0.5Al_2O_3 + 2SiO_2 \rightarrow CsAlSi_2O_6 + 0.5H_2O$$
$$RbOH + 0.5Al_2O_3 + 2SiO_2 \rightarrow RbAlSi_2O_6 + 0.5H_2O$$
$$Sr(OH)_2 + Al_2O_3 + 2SiO_2 \rightarrow SrAl_2Si_2O_8 + H_2O$$
$$3Ba(OH)_2 + BaI_2 + 3Al_2O_3 + 6SiO_2 \rightarrow Ba_4(AlSiO_4)_6I_2 + 3H_2O$$
$$3Ba(OH)_2 + BaBr_2 + 3Al_2O_3 + 6SiO_2 \rightarrow Ba_4(AlSiO_4)_6Br_2 + 3H_2O$$
$$Ba(OH)_2 + Al_2O_3 + 2SiO_2 \rightarrow BaAl_2Si_2O_8 + H_2O$$

Hydrogen is separated from argon in the off-gas from the sparge, then catalytically combined with oxygen to provide process heat.

The dried minerals are combined with 10–25% excess $Al_2O3 \cdot 4SiO_2$ and loaded into Hastelloy-N capsules that have a 143 mm Graded-Z shield, then packed using vibro-compacting, for disposal as high level waste using "salt divers," as recommended by Charles Forsberg [22]. If lanthanides are processed by the the chloride method, the resulting lanthanide-analog monazite is included. Decay heat of the iodine, caesium, and strontium fractions facilitates the autonomous descent of self-sinking capsules through the halite medium to the base of a six-kilometer salt dome, ensuring permanent geological sequestration far below the horizon of human access or concern. In the context

of eternal storage in halite domes, the Hastelloy-N capsules can be considered a sacrificial barrier that most likely lasts far longer than the time required for the most significantly radiotoxic isotopes, caesium and strontium, to decay to insignificant levels with their ≈ 30 year half lives.

Molybdenum, InPd, zirconium intermetallic compounds from the cadmium dissolver overflow, and scrap iron are combined, then melted into ingots, as was done for noble metal processing at EBR-II. If lanthanides are separated as metals in the 775 K stage, they are included in the alloy. If technetium transmutation to ruthenium and rhodium is not profitable, it is included in the alloy.

Noble metals that do not meet purity specifications for immediate market release are consolidated into ingots and stored as low-level radioactive waste.

Inert gas fission products — krypton and xenon — are stored in conventional compressed gas cylinders. They have the advantages that they have relatively short half lives (10.75 y and 36.40 d), and their decay products are not radioactive, except for ^{85}Br, which has a half life of 2.9 seconds. After the radioactive isotopes decay sufficiently, remaining gases can be sold or simply released to the atmosphere.

The processing goal is that, altogether, the actinide concentration in the produced waste is ≈ 1 ppm.

Direct disposal of spent oxide fuel must deal with enormously larger volumes, not least because only $\approx 5\%$ of the mass is fission products; the remainder is valuable unused fuel.

After pyroprocessing at EBR-II, many fission products remained in electrolyte. Electrolyte was cleansed by passing through a column of Zeolyte-A. It occluded significant amounts of electrolyte, and did a rather poor job of removing caesium [1]. The final waste form was produced by mixing the contaminated Zeolyte-A with glass frit and compression melting to form a sodalite-glass composite. Total fission product density was low. This is a legally accepted waste form, but it is not a mineral; it is a cage for salts. It is probably sufficient to prevent any harm, but ceramic minerals are superior. Although the pyroprocessor at EBR-II produced a much smaller volume of waste than would disposing of unprocessed spent fuel, the method proposed here produces a still more significantly smaller volume.

The proposed method, and pyroprocessing, are both superior to immiscible solvent processing such as PUREX, which would be largely irrelevant for metallic fuel.

As a result of fuel processing and waste preparation, the IMFR achieves a closed-loop waste cycle that produces much smaller and segregated waste volumes, thereby minimizing both shipping volume and leveraging different storage requirements to minimize long-term storage and monitoring costs.

II.6 Processing Breeder Particles

If breeding is desired and the alloy is not changed to accomplish it, either "snap on" axial breeding blankets or radial hybrid elements that replace shield/reflector elements in the periphery of the reactor core can be used.

Radial hybrid breeder elements would be connected to the fuel processor in the same way as fuel elements, but using a parallel slurry-transport return tube, connected only to these elements, to avoid putting fuel particles containing fissionable TRU into breeder elements.

Axial breeders would be processed in batches by physically removing the "snap on" cartridges and

gradually removing particles from them in the fuel processing hall using an eductor to produce the same sort of ≈7.8% slurry.

The fuel processor does not need a separate stream to process breeder particles.

II.7 Fuel Reconstitution

Zirconium forms refractory intermetallic compounds with fission products, and more zirconium forms those compounds than arises as a fission product. If ZrAn compounds cannot be sufficiently purely recovered and used, about 24.3 grams of replacement hafnium-free zirconium are required per MWe-year, ≈7.5 kg/yr for the 840 MWth IMFR. Actinides from the fuel processing system, including AnZr intermetallic compounds, are combined with additional depleted uranium and replacement zirconium, and melted in an induction furnace at 1450–1550 K.

Sodium vapor is produced in a shell around the induction furnace. The melt flows from the bottom of the furnace to an atomizer powered by high-pressure sodium vapor, to produce 50 µm particles. The high-temperature sodium vapor from this process is used throughout the processor for any heat that is required at higher temperatures than secondary sodium coolant.

The particles fall into a sodium pool where they settle under the influence of gravity to form a ≈78% settled bed. An eductor powered by motive sodium strips a ≈7.8% slurry, which is combined with the returning slurry of unprocessed particles. If the return venturi does not provide sufficient pressure gradient, the combined slurry is pressurized by an electromagnetic pump to return the slurry to the reactor.

The particle atomizer will have a pulsed cycle because it cannot work reliably at 14 g min^{-1}. Even 840 g h^{-1} might be too slow, but 20 kg d^{-1} (1.2 L d^{-1}) is certainly workable.

Table II.5 shows that more zirconium is removed as refractory intermetallic compounds with fission products than the amount of zirconium fission product.

Table II.5: Zirconium Inventory

Element	Compound	Element Mole %	Zirconium Mole %
Antimony	Zr_5Sb_3	0.05	0.083
Arsenic	Zr_3As	<0.005	<0.005
Gallium	Zr_5Ga_3	<0.005	<0.005
Germanium	Zr_5Ge_3	2.97	4.95
Palladium	$ZrPd_3$	4.88	1.63
Rhodium	$ZrRh_3$	1.30	0.43
Ruthenium	ZrRu	7.51	7.51
Selenium	ZrSe	0.24	0.24
Silver	$AgZr_2$	0.24	0.48
Tellurium	ZrTe	1.28	1.28
Tin	Zr_5Sn_3	0.26	0.43
Total		18.73	17.04
Zirconium	Zr		13.11

It might be desirable to recycle ZrRu from the 1000 K stage to offset the cost of fresh hafnium-free

zirconium. Whether that is possible depends upon whether replacing 11% zirconium with 5.5% zirconium and 5.5% ruthenium — the equilibrium condition — is viable. Preliminary studies using OpenMC suggest $k_{\text{eff}} \approx 1.0$ and BR ≈ 1.0 are possible by using more TRU, which would require an increase in breeding ratio, beyond the increase required to compensate for increasing burnup (see Table I.6), until equilibrium is reached. Increasing ruthenium reduces thermal conductivity and ductility. Experiments are required to determine the total impact. There might be a small market for excess zirconium intermetallic compounds if the cost to separate zirconium is less than the cost to separate hafnium from native zirconium.

To create particles for breeding, uranium harvested in the processing hall would be mixed with fresh ^{238}U. If U-10Zr alloy is needed instead of pure uranium, zirconium is added. A separate melting furnace and separate system of atomizers is used because there must be much less plutonium and other TRU in breeder elements.

Part III

Conclusion

The Integral Mobile-fuel Fast Reactor (IMFR) is inherently "walk-away" safe. It operates continuously with no need for periodic refueling shutdowns, contains very few moving parts, and integrates a continuous on-site fuel processor. The entire system forms a nearly closed, autonomous loop. All fissile material and depleted uranium required for its century-long service life, less than $2\,\text{m}^3$, along with initial inventories of argon, cadmium, and sodium, are delivered at startup. During operation, the only inputs are low-cost consumables: alumina, silica, scrap iron, minor makeup of argon/cadmium/sodium, and ammonium phosphate (if the alternative lanthanide process is used).

Outputs are limited to:

- Fission gases, stored on-site until they decay and can be released at end-of-life.
- Compact mineralized waste forms (pollucite, slawsonite/strontium-anorthite, celsian, yttrium aluminum garnet, and monazite if alternative lanthanide processing is required, with alumina and silica) in Hastelloy-N salt divers, with total actinide carry-over targeted at ≈ 1 ppm.
- Lanthanide-molybdenum-zirconium-iron ingots.
- Noble metal ingots or powders, which might represent a revenue stream rather than a disposal cost.
- Excess transuranics (primarily plutonium) for startup of additional fast reactors if a breeding ratio greater than 1.0 is employed.

The IMFR concept represents a broader system than a simple electricity generator. Although its initial capital cost likely exceeds that of open-cycle plants, it directly addresses many of the nuclear industry's most significant — yet often unaccounted — economic challenges. When evaluated on a complete-system basis, the IMFR's economic viability arises from its integrated, closed fuel cycle and century-scale service life. Unlike light-water reactors, which are exposed to volatile external fuel-cycle costs, transport logistics, and substantial long-term liabilities for managing unprocessed

spent fuel, the IMFR decouples energy production from these dependencies. Modular element replacement avoids large capital shocks, the continuous pyrochemical processor eliminates external fuel fabrication and transport, and segregated high-density mineralized waste forms dramatically reduce repository requirements and monitoring burdens.

With roughly 90,000 tonnes of existing spent nuclear fuel and 900,000 tonnes of depleted uranium in the United States, fast-spectrum metallic-fuel systems with on-site processing could power an all-electric U.S. economy (estimated demand $\gtrsim$1,600 GWe) for over 500 years without mining, milling, refining, enriching, or importing one new gram of uranium. The IMFR is well-positioned as a key component of such a fleet.

While initially intended for baseload electricity, the high-temperature sodium pool and integrated processing hall also provide a robust platform for process heat, and thermochemical applications such as hydrogen production.

Although the concept builds upon extensive EBR-II experience, critical aspects — particularly the rheological behavior of the high-volume-fraction metallic paste and long-term system performance — require experimental validation. Targeted laboratory tests, coupled modeling, and eventual small-scale prototyping will be essential before full-scale deployment. The IMFR represents a promising pathway toward safer, more sustainable, and economically resilient nuclear energy.

Part IV

Future Investigations

IV.1 Future Work and Open Investigations

The IMFR concept presented here is exploratory. Substantial further research, development, and demonstration in several critical areas are required to realize the design.

Fuel Circulation and Slurry Behavior All wetted surfaces are coated with $>10\,\mu$m W-10Ta to withstand forty years of abrasion. Experiments using depleted uranium simulant paste (without transuranics) are required to verify long-term performance. Key uncertainties include Bingham plastic behavior at $\approx 78\%$ volume mixing ratio, potential "hiccups" or "chugging" in the circulation system, startup of upcomer channels initially filled with paste, and the pressure required to clear such slugs. Several startup schemes (brute-force modulation, parallel perforated channels, etc.) should be evaluated. Self-sintering risk at homologous temperatures ≈ 0.7 must be quantified; mitigation options include fluidic oscillators in coolant tubes or alternative fuels (e.g., mononitride).

Thermal-Hydraulic and Neutronic Parametric Studies Detailed coupled 3D neutronic-thermal-hydraulic transient analyses are needed to quantify passive safety margins (axial expansion feedback, unprotected transients, seismic response) in detail. The effect of grid plate flexibility and full-core seismic interaction should be included. Fuel paste volume fraction versus number of coolant tubes should be optimized for a target peak temperature.

Continuous Fuel Processing The cadmium-based fractional crystallization cascade requires engineering-scale demonstration, particularly regarding materials compatibility under irradiation, criticality control in hydrocyclones, long-term diafilter performance, and overall process stability. Alternative paths (e.g., initial dissolution as a precursor to pyroprocessing) should be pursued in parallel.

Materials and Component Life Long-term irradiation, creep, and abrasion testing of RAFM structures, W-15Cr-8Fe-5Hf shielding, and HIP bonds is essential to confirm the 40-year element lifetime.

Economic, Regulatory, and Scaling Studies Refined FOAK/NOAK cost models, supply chain development for specialized materials, and a licensing pathway for a mobile-fuel reactor with on-site continuous processing are required. Scalability to different power levels and regional fuel-recycling services should be explored.

More detailed experimental plans, modeling requirements, and parametric studies are provided in Appendix I.

Part V

Acknowledgments

The author wishes to express profound gratitude for the technical guidance and patient mentorship provided by **Dr. Yoon Il Chang** during the preceding twenty years, and earlier but sadly brief mentorship provided by the late **Dr. George Stanford**. Their foundational knowledge of every aspect of the Integral Fast Reactor (IFR) program, metallic-fuel physics, pyroprocessing, and weapons-proliferation avoidance, and their eagerness to share it, was essential to the development of this monograph.

Declaration of generative AI and AI-assisted technologies in the manuscript preparation process

The author gratefully acknowledges assistance from online tools, including AI tools such as Google Gemini, Grok, Claude, and Alter to aid in literature search, spelling and grammar checking, and LaTeX formatting. Some were asked to pretend to be professional journal referees, and offered valuable criticism. AI tools were not used for composition or diagram preparation. Principles of analysis and fundamental ideas are the author's alone.

References

[1] J.P. Ackerman, R.W. Benedict, J.E. Herceg, K.M. Johnson, L.C. Layman, and W.E. Miller. Treatment of wastes in the Integral Fast Reactor (IFR) fuel cycle. *Progress in Nuclear Energy*, 31(1-2):141–154, 1997.

[2] American Nuclear Society. *Status of Fuel Element Modeling Codes for Metallic Fuels*, Tucson, AZ, Sep 1986.

[3] R. E. Aven and G. T. Trammell. Homogeneous reactor project quarterly progress report. Technical Report ORNL-1221, Oak Ridge National Laboratory, November 1951.

[4] J. E. Battles, W. E. Miller, and E. C. Gay. Pyrometallurgical processing of Integral Fast Reactor metal fuels. *Progress in Nuclear Energy*, 26(3):345–351, 1991.

[5] David Baurac. Passively safe reactors rely on nature to keep them cool. *Logos – Pioneering Science and Technology*, 20(1), Winter 2002.

[6] W. G. Blessing, S. D. Bowers, R. J. Hennig, P. R. Huebotter, W. H. Jens, E. C. Kovacic, F. J. Leitz, C. R. Moore, and F. P. Storrer. Conceptual design of a 300 MWe paste-fueled fast breeder power reactor. Technical Report APDA-146, Atomic Power Development Associates, 1911 First Street, Detroit, Michigan 48226, October 1961.

[7] Klaus Borho, Jörg Heilek, and Gunter Schnabel. Separation of liquid eutectic mixtures by crystallization on cold surfaces and apparatus for this purpose, September 1998. U. S. Patent number 5,814,231.

[8] Klaus-Joachim Borho. Phasengleichgewichte in den Systemen Lithiumchlorid-Caesiumchlorid und Lithiumchlorid-Rubidiumchlorid. *Chemische Berichte*, 103(11):3645–3651, 1970. Borho Method for alkali metal halide separation.

[9] D. A. Brown, M. B. Chadwick, R. Capote, A. C. Kahler, A. Trkov, M. W. Herman, A. A. Sonzogni, Y. Danon, A. D. Carlson, M. Dunn, D. Parsons, G. M. Hale, G. Voyles, M. Cowan, B. Bates, C. Frankle, A. Kahler, C. Mattoon, B. Pritychenko, M. Romjue, E.Simpson, B. Sleaford, V. Sobes, P. Vackar, and M. Zerkle. ENDF/B-VIII.0: The 8th Major Release of the Nuclear Reaction Data Library of the Cross Section Evaluation Working Group (CSEWG). *Nuclear Data Sheets*, 148:1–142, 2018.

[10] D. A. G. Bruggeman. Berechnung verschiedener physikalischer Konstanten von heterogenen Substanzen. I. Dielektrizitätkonstanten und Leitfähigkeiten der Mischkörper aus isotropen Substanzen [Calculation of various physical constants of heterogeneous substances. I. Dielectric constants and conductivities of mixtures of isotropic substances.]. *Annalen der Physik*, 416(7):636–664, 1935.

[11] John Burkardt. FEM2D_Poisson_CG: Finite element method for the 2D Poisson equation. https://people.sc.fsu.edu/~jburkardt/c_src/fem2d_poisson_cg/fem2d_poisson_cg.html, 2026. Accessed: 2026-06-07.

[12] Y. I. Chang, L. C. Walters, J. E. Battles, D. R. Pedersen, D. C. Wade, and M. J. Lineberry. Integral Fast Reactor program summary progress report, FY 1985–FY 1989. Technical Memorandum ANL-IFR-125, Argonne National Laboratory, Argonne, IL, 1990.

[13] Shoei-Sheng Chen. Flow-induced vibration of circular cylindrical structures. Report ANL-85-51, Argonne National Laboratory, Argonne, IL, June 1985. Available at https://inldigitallibrary.inl.gov/Reports/ANL-85-51.pdf.

[14] Shoei-Sheng Chen. *Flow-Induced Vibration of Circular Cylindrical Structures*. Hemisphere Publishing, 1987.

[15] R. J. DiMelfi and J. M. Kramer. Modelling the effects of grain-boundary fission gas on transient fuel behavior. *Nuclear Technology*, 50(1):25–33, 1980.

[16] Thaddeus B. Massalski (Editor-in-Chief), Joanne L. Murray, Lawrence H. Bennett, Hugh Baker (Editors), and Linda Kacprzak (Associate Editor). *Binary Alloy Phase Diagrams*. American Society for Metals, Metals Park, Ohio 44073, 1986. ISBN 0-87170-261-4.

[17] A. Einstein. Eine neue Bestimmung der Moleküldimensionen. *Annalen der Physik*, 19(2):289–306, 1906.

[18] A. Einstein. Berichtigung zu meiner Arbeit: "Eine neue Bestimmung der Moleküldimensionen". *Annalen der Physik*, 34(3):591–592, 1911.

[19] Robert S. Farr and Robert D. Groot. Close packing density of polydisperse hard spheres. *Journal of Chemical Physics*, 131, 2009.

[20] Tingzhou Fei, Barbara Vezzoni, Marco Marchetti, Willem Frederik Geert van Rooijen, and Ye Zhang. Neutronics benchmark for EBR-II shutdown heat removal test SHRT-45R. In *Proceedings of the International Conference on Physics of Reactors (PHYSOR 2016)*, pages 221–230, Sun Valley, Idaho, USA, 2016.

[21] Joanne K. Fink and Leonard Leibowitz. Thermodynamic and transport properties of sodium liquid and vapor. Technical Report ANL-RE-95/2, Argonne National Laboratory, 9700 Cass Avenue, Argonne, Illinois 60440, January 1995.

[22] Charles W. Forsberg. Rethinking high-level waste disposal: Separate disposal of high-heat radionuclides (^{90}Sr and ^{137}Cs). *Nuclear Technology*, 131(2):252–268, 2000.

[23] Sho Fuchita, Koji Fujimura, Daisuke Watanabe, Hirotaka Nakahara, Kazuhiko Matsumura, Hirokazu Ohta, and Masatoshi Iizuka. Core concept of innovative small SFR with metal fuel for deployment in Japan. *Progress in Nuclear Science and Technology*, 7:20–26, 2025.

[24] C. C. Furnas. Grading aggregates I: Mathematical relations for beds of broken solids of maximum density. *Industrial & Engineering Chemistry*, 22(9):1207–1211, 1930.

[25] Ian Gibson, David Rosen, Brent Stucker, and Mahyar Khorasani. *Additive Manufacturing Technologies: 3D Printing, Rapid Prototyping, and Direct Digital Manufacturing*. Springer, Cham, Switzerland, 3rd edition, 2021.

[26] Volker Hessel, Steffen Hardt, and Holger Löwe. *Micro Process Engineering: Fundamentals, Devices, Fabrication, and Applications*. Wiley-VCH, Weinheim, Germany, 2004.

[27] Celene Hin, Dane Morgan, Jianguo Yu, and Cynthia Papesh. Thermal conductivity of metallic uranium. Technical Report NEUP 14-6767, Virginia Tech, 2018.

[28] G. L. Hofman, L. Leibowitz, J. M. Krame, M. C. Billone, and J. F. Koenig. Metallic fuels handbook. Technical Report ANL-IFR-29, Argonne National Laboratory (ANL), 1985. Available via OSTI ID: 712317.

[29] G. L. Hofman, L. C. Walters, and T. H. Bauer. Metallic fast reactor fuels. *Progress in Nuclear Energy*, 31(1/2):83–110, 1997.

[30] IEEE. IEEE Standard for Seismic Qualification of Equipment for Nuclear Power Generating Stations. Technical Report IEEE Std 344-2013, Institute of Electrical and Electronics Engineers, 2013.

[31] Irving Johnson. The thermodynamics of pyrochemical processes for liquid metal reactor fuel cycles. Technical Report ANL-87-44, Argonne National Laboratory, Argonne, IL, 1987.

[32] Leonard J. Koch. *EBR-II: Plus 25: A Memoir*. American Nuclear Society, La Grange Park, IL, 1988.

[33] I. M. Krieger and T. J. Dougherty. A mechanism for non-Newtonian flow in suspensions of rigid spheres. *Transactions of the Society of Rheology*, 3(1):137–152, 1959.

[34] A. Kruizenga and et al. Printed circuit heat exchanger (PCHE) design and performance assessment for high temperature applications. Technical Report SAND2016-XXXX, Sandia National Laboratories, 2016.

[35] R. N. Lyon. Preliminary report of the 1953 Los Alamos boiling reactor experiments. Technical Report CF-53-11-65, Oak Ridge National Laboratory, November 1953. Declassified 14 February 1957.

[36] Maplesoft, a division of Waterloo Maple Inc. *Maple, Version 2020*. Maplesoft, a division of Waterloo Maple Inc., Waterloo, Ontario, Canada, 2020.
https://www.maplesoft.com/.

[37] R. K. McGeary. Mechanical packing of spherical particles. *Journal of the American Ceramic Society*, 44(10):513–522, 1961.

[38] Paul K. Romano, Nicholas E. Horelik, Bryan R. Herman, Adam G. Nelson, Benoit Forget, and Kord Smith. OpenMC: A state-of-the-art Monte Carlo code for research and development. *Annals of Nuclear Energy*, 82:90–97, 2015.

[39] J. I. Sackett. Operating and test experience with EBR-II, the IFR prototype. *Progress in Nuclear Energy*, 31(1/2):111–130, 1997.

[40] Christian Schiele. On an improved form of thrust bearing. *Proceedings of the Institution of Mechanical Engineers*, 4(1):20–25, 1853.

[41] A. Yu. Shadrin, A. G. Osipenko, I. B. Shirokov, V. I. Volk, S. N. Veselov, and K. N. Dvoyeglazov. PH process as a technology for reprocessing mixed uranium–plutonium nitride fuel. *Radiochemistry*, 58(3):317–321, 2016.

[42] Jonathan Richard Shewchuk. Triangle: Engineering a 2D quality mesh generator and Delaunay triangulator. In Ming C. Lin and Dinesh Manocha, editors, *Applied Computational Geometry: Towards Geometric Engineering*, volume 1148 of *Lecture Notes in Computer Science*, pages 203–222. Springer-Verlag, Berlin, 1996.

[43] W. Van Snyder. Finely divided metal as nuclear reactor fuel. *Nuclear Technology*, 208(9):1416–1432, 2022.

[44] W. Van Snyder. Revisiting mobile paste reactor fuel. *Nuclear Technology*, 210(3):342–358, 2024.

[45] W. Van Snyder. Conceptual proposal: Reactor cooled by high-temperature sodium vapor. *Nuclear Technology*, 2026.

[46] J. M. Stein and Paul Rudolph Kasten. Boiling reactors: A preliminary investigation. Technical Report ORNL-1062, OSTI 4338553, Oak Ridge National Laboratory, December 1951. Declassified 2 March 1957.

[47] ORNL Team. ASME code considerations for compact heat exchangers, 2015. ORNL Report on diffusion-bonded designs.

[48] Charles E. Till and Yoon Il Chang. *Plentiful Energy: The Story of the Integral Fast Reactor*. CreateSpace Independent Publishing Platform, Charleston, SC, 2011.

[49] Brian S. Triplett, Eric P. Loewen, and Brent J. Dooies. PRISM: A competitive small modular sodium-cooled reactor. *Nuclear Technology*, 178(5):186–200, May 2012.

[50] Barbara Vezzoni, Willem Frederik Geert van Rooijen, Tingzhou Fei, Ye Zhang, Marco Marchetti, Paolo Balestra, and Carlo Parisi. IAEA neutronics benchmark for EBR-II SHRT-45R. Technical Report IAEA-CN245-070, IAEA.

Appendix A. Thermal analysis

A two-dimensional analysis using the steady-state heat equation, *viz.*

$$\nabla \cdot (\kappa \nabla T) + Q = 0 \tag{A.1}$$

was conducted in an axial slice between coolant tubes with $z \gg r$, where T is temperature, κ is thermal conductivity, and Q is internal heat production. The region is slightly simplified from an axial section of the fuel element by having a horizontal bottom (the ridge of the hopper) instead of the region being a trapezoid (the valley of the hopper). The intent of this study is not a detailed analysis of axial temperature distribution. Rather, it is to confirm that with Dirichlet conditions at the top and bottom, Robin conditions at the vertical edges, linearly increasing coolant temperature along the edges, and uniform heat production (Q), axial temperature variation is nearly linear, with slope very nearly equal to the coolant tubes' temperature gradient, except very near the top and bottom, where temperature returns quickly to the Dirichlet condition. A more detailed analysis would use the power profile from a full-core nuclear power and thermal analysis. Although this would produce the typical central-level-peak cosine power profile, the temperature gradient remains locally linear, and the average gradient would be similar to the average coolant temperature gradient.

With the conjecture of linear axial temperature variation verified, a detailed specification of a horizontal section was constructed. With linear axial temperature gradient the second-derivative axial term in the Laplacian $\left(\frac{\partial^2 T}{\partial z^2}\right)$ is zero. The simplified problem is colloquially called a *2.5 dimensional* equation. Even though the computational problem has been simplified, the physical problem remains a three-dimensional problem. It is solved, physically, as a 1 mm thick slice, under the assumption that the axial temperature gradient is almost exactly the specified $\frac{\partial T}{\partial z}$, and that the change is sufficiently small that the solution represents temperature throughout the 1 mm slice with $<0.1\,\mathrm{K\,mm^{-1}}$ axial variation from the mean.

In addition to the geometric shape of the cross section, the following were included in the model:

- Thickness of tube walls and duct walls.
- Thermal conductivity of structural steel.
- Thermal conductivity of fuel paste.
- Density, heat capacity, and velocity of coolant flow.
- Velocity of fuel paste flow.

When temperature-dependent thermal conductivity is allowed in the heat equation (A.1) it becomes nonlinear because of the temperature dependence of conductivity $\kappa(T)$.

$$\kappa(T)\,\nabla^2 T + \nabla\kappa(T) \cdot \nabla T + Q = \kappa(T)\,\nabla^2 T + \|\nabla T\|^2\,\frac{\partial \kappa(T)}{\partial T} + Q = 0 \tag{A.2}$$

where the second form is obtained by applying the chain rule to $\nabla\kappa(T)$. ∇T is the full 3-dimensional gradient, taking advantage of knowing the specified value of $\frac{\partial T}{\partial z}$. $\nabla_{xy} T$ is calculated at each node

using either an area-weighted average of $\nabla_{xy} T$ in each triangle containing the node where it is needed, or by fitting a plane to the temperature at adjacent nodes using a least-squares method, where the node is weighted heavily and adjacent nodes are weighted according to the inverse of their distance. The results using these two methods were nearly identical.

In addition to using the specified $\frac{\partial T}{\partial z}$ in ∇T, the axial dimension is incorporated as convective heat transfer into the internal heat term Q using

$$Q_{\text{eff}} = Q_{\text{vol}} - \rho \, C_p \, u_z \, \frac{\partial T}{\partial z}$$

where ρ is temperature-dependent fuel paste density, C_p is temperature-dependent fuel paste heat capacity, u_z is fuel paste axial velocity ($\approx 0.09\,\text{mm}\,\text{s}^{-1}$), and $\frac{\partial T}{\partial z}$ is the specified vertical temperature gradient verified by the first study.

The geometry is discretized using triangulation by Jonathan Shewchuk's *Triangle* package [42]. The statistics are reported in Table A.1.

Table A.1: Mesh Statistics

Vertices	Triangles	Edges	Exterior Boundary Edges
24915	44601	69786	5769

Structural elements are not modeled directly as part of the geometry because they are very thin. Their thermal properties are included in the Robin boundary conditions.

The equation is solved using John Burkardt's *FEM2D_Poisson_CG* finite element package [11], modified by the author to use Fortran 2003 facilities for object-oriented programming, and to incorporate support for Robin boundary conditions. Robin boundary conditions are a weighted combination of Dirichlet and Neumann boundary conditions, written abstractly as

$$\alpha \, T + \beta \, \nabla T \cdot \mathbf{n} = \alpha \, T + \beta \, \frac{\partial T}{\partial \mathbf{n}} = g \, , \tag{A.3}$$

where $\mathbf{n}$ is the outward normal at the boundary.

Robin boundary conditions are incorporated into the finite-element equation in two places by adding

$$\text{BC}_{\text{diag}} = W_{\text{edge}} \, h_R \tag{A.4}$$

to the diagonal of the stiffness matrix, where the edge weight W_{edge} is the sum of half the lengths of the edges along the boundary incident on the boundary node, and by adding

$$\text{BC}_{\text{RHS}} = \text{BC}_{\text{diag}} \, T_{\text{coolant}} \tag{A.5}$$

to the right-hand size of the equation.

At the interface, the heat flux leaving the fuel domain equals the heat passing through the combined wall-and-fluid thermal network:

$$-\kappa \frac{\partial T}{\partial n} = -\kappa(T)\, \nabla(T) \cdot n = h_R(T)\, (T_{\text{fuel}} - T_{\text{coolant}}) \tag{A.6}$$

To account for finite wall thickness (t_{wall}) and metal conductivity (κ_{wall}) in series with the fluid film convection (h_{fluid}), compute the Robin heat convection term:

$$\frac{1}{h_R} = \frac{t_{\text{wall}}}{\kappa_{\text{wall}}(T_{\text{avg}})} + \frac{1}{h_{\text{fluid}}}\,, \tag{A.7}$$

where T_{avg} is the average of fuel and coolant temperature at the boundary node, h_{fluid} is the heat convection coefficient in coolant:

$$h_{\text{fluid}} = \frac{\text{Nu}\, \kappa_{\text{Na}}(T)}{D_h}\,, \tag{A.8}$$

$\kappa_{\text{Na}}(T)$ is coolant thermal conductivity, D_h is the hydraulic diameter (described in Section I.1.6 and Appendix B), Nu is the Nusselt number

$$\text{Nu} = 5.0 + 0.025\, \text{Pe}^{0.8}\,, \tag{A.9}$$

Pe is the Péclet number, a dimensionless number characterizing the ratio of convective to conductive transport,

$$\text{Pe} = \frac{\rho\, v\, D_h\, C_p(T)}{\kappa_{\text{Na}}}\,, \tag{A.10}$$

$C_p(T)$ is sodium heat capacity at constant pressure, and v is coolant velocity (described in Section I.1.6).

Sodium density ρ, heat capacity $C_p(T)$, and conductivity $\kappa_{\text{Na}}(T)$ are calculated at the film temperature, the average of fuel and coolant temperature [21].

The finite element equation is very sparse, and is solved by the *Conjugate Gradient* method. When temperature-dependent conductivity, density, and heat capacity are incorporated, the heat equation becomes nonlinear. It is solved using a Picard iteration (also known as a fixed-point iteration) that converges remarkably quickly; a Newton iteration was not necessary.

As can be observed in Figure I.1, the spaces between the outermost ring of coolant tubes and the duct wall are not of the same shape as interior spaces between coolant tubes. This results in alternating hot and cold regions along the duct wall. The heat equation solution is iterated to change δ in Figure I.1 until the average of the maximum temperatures in the hot spaces between coolant tubes and the outer wall is within 0.1 K of the average of the maximum temperatures in the regions between coolant tubes in the outermost two rings. The result is that the ratio δ/s in Figure I.1 is ≈ 0.57. This iteration also converges remarkably quickly. Using only one core of an Intel 14990K processor, the processing time was about eleven seconds.

Appendix B. Coolant Hydraulic Analysis

Hydraulic analysis for the 271-tube case began by ensuring that the temperatures of coolant emerging from the tops of coolant tubes are nearly equal to each other and nearly equal to the temperature of coolant emerging from the tops of areas, called *jackets* below, around fuel elements. If this is not so, thermal striping occurs above the core. This required consideration of the *hydraulic diameters* of different coolant-flow regions, due to their different shapes. The hydraulic diameter affects cooling efficiency. The hydraulic diameter D_h is defined as

$$D_h = \frac{4A_{\text{flow}}}{P_{\text{wetted}}}\,. \tag{B.1}$$

where A_{flow} is the cross-sectional flow area, and P_{wetted} is the corresponding wetted perimeter. For a circular tube, D_h is its diameter.

For a regular hexagonal coolant tube with flat-to-flat inner width η,

$$D_{h,\text{tubes}} = \frac{4\left(\frac{\sqrt{3}}{2}\eta^2\right)}{2\sqrt{3}\eta} = \eta\,. \tag{B.2}$$

For a thin rectangular slab (the outer bypass jacket channel) of width W and thickness τ, the flow area is $A_{\text{flow}} = W\,\tau$ and the wetted perimeter is $P_{\text{wetted}} = 2(W + \tau)$. Therefore

$$D_{h,\text{jacket}} = \frac{2\,W\,\tau}{W + \tau}\,. \tag{B.3}$$

Pressure drops in channels are related to velocity by the Darcy-Weisbach relation (an extension of Bernoulli's principle that incorporates friction):

$$\Delta P = f\frac{L}{D_h}\frac{\rho v^2}{2}\,. \tag{B.4}$$

For fully developed turbulent flow in smooth channels, the friction factors are described by the Blasius correlation:

$$f = C\,\text{Re}^{-0.25} = C\left(\frac{\rho\,v\,D_h}{\mu}\right)^{-0.25}\,. \tag{B.5}$$

where Re is the Reynolds number, the Blasius coefficient $C \approx 0.3164$, and μ is the dynamic viscosity of the fluid.

Substituting the friction factor into the pressure drop Equation (B.4) yields:

$$\Delta P = C\left(\frac{\rho v D_h}{\mu}\right)^{-0.25}\frac{L}{D_h}\frac{\rho v^2}{2} = \left[C\left(\frac{\rho}{\mu}\right)^{-0.25}\frac{L\rho}{2}\right]v^{1.75}D_h^{-1.25}\,. \tag{B.6}$$

Because the internal tubes and outer jacket channels are connected in parallel between shared inlet and outlet plenums, their pressure drops are necessarily equal ($\Delta P_{\text{jacket}} = \Delta P_{\text{tubes}}$). Canceling identical factors simplifies the velocity ratio to a function of the hydraulic diameters alone:

$$\frac{v_{\text{jacket}}}{v_{\text{tubes}}} = \left(\frac{D_{\text{h,jacket}}}{D_{\text{h,tubes}}}\right)^{\frac{1.25}{1.75}} = \left(\frac{D_{\text{h,jacket}}}{D_{\text{h,tubes}}}\right)^{\frac{5}{7}} . \tag{B.7}$$

Assuming the thermal design criteria require matching bulk fluid energy carrying capacity to the cross-sectional mass flow distribution ($q \propto Av$), equalizing the total heat removal rates ($q_{\text{jacket}} = q_{\text{tubes}}$) requires:

$$\frac{q_{\text{jacket}}}{q_{\text{tubes}}} = \frac{A_{\text{jacket}}}{A_{\text{tubes}}}\frac{v_{\text{jacket}}}{v_{\text{tubes}}} = \frac{A_{\text{jacket}}}{A_{\text{tubes}}}\left(\frac{D_{\text{h,jacket}}}{D_{\text{h,tubes}}}\right)^{\frac{5}{7}} = 1 . \tag{B.8}$$

This establishes the final self-consistent fluid dynamic area relationship for the geometric design:

$$\frac{A_{\text{tubes}}}{A_{\text{jacket}}} = \left(\frac{D_{\text{h,tubes}}}{D_{\text{h,jacket}}}\right)^{-\frac{5}{7}} = \left(\frac{\eta(W+\tau)}{2\,W\,\tau}\right)^{-\frac{5}{7}} . \tag{B.9}$$

The heat removal rate depends upon velocity, temperature drop, and heat capacity:

$$\dot{Q} = \dot{m} C_p \Delta T = \rho(A_{\text{tubes}}\, v_{\text{tubes}} + A_{\text{jacket}}\, v_{\text{jacket}})\, C_p \Delta T . \tag{B.10}$$

The area and velocity ratios cancel if the jacket quantities are substituted, giving

$$\dot{Q} = 2\,\rho\, A_{\text{tubes}}\, v_{\text{tubes}}\, C_p\, \Delta T , \tag{B.11}$$

from which

$$v_{\text{tubes}} = \frac{\dot{Q}}{2\,\rho\, A_{\text{tubes}}\, C_p\, \Delta T} . \tag{B.12}$$

Appendix C. Fuel Alloy Migration

Two effects, Fickian diffusion and Ludwig-Soret drift, compete according to the following relation [29, Eq. 2]:

$$J_i = -D_i \left(\nabla C_i + C_i \frac{Q_i^*}{R_g T^2}\nabla T\right) , \tag{C.1}$$

where

- J_i (atoms/barn/s) is the atom flux of alloy constituent i.
- D_i ($\text{m}^2\ \text{s}^{-1}$) is the atomic diffusion coefficient for constituent i.
- C_i (atoms/barn-cm) is the concentration of constituent i.

- Q_i^* is the heat of transport (the parameter dictating a species' thermodynamic tendency to move toward hotter or colder regions) for constituent i.
- R_g is the universal gas constant $8.314\,\mathrm{J\,mol^{-1}\,K^{-1}}$.
- T is temperature.

If a concentration gradient develops, it opposes the Ludwig-Soret effect, with

$$\nabla C_i \approx -C_i \frac{Q_i^*}{R_g T^2} \nabla T \,. \tag{C.2}$$

The change in concentration is the divergence of flux, *viz.*

$$\frac{\partial C_i}{\partial t} = -\nabla \cdot J_i \,. \tag{C.3}$$

Substituting this into Equation (C.1) we have

$$\frac{\partial C_i}{\partial t} = D_i \nabla^2 C_i + D_T \frac{Q_i^*}{R_g} \nabla \cdot \left(\frac{C_i}{T^2} \nabla T \right) , \tag{C.4}$$

wherein the first term is Fickian diffusion, the second is Ludwig-Soret drift, and D_T is the thermal diffusion coefficient.

In the radial direction, the temperature within particles varies as

$$\frac{\partial T}{\partial r} = -\frac{Qr}{3\kappa} \,. \tag{C.5}$$

The temperature derivative at the center is zero, from which.

$$T_{\text{center}} = T_s + \frac{QR^2}{6\kappa} \,,$$

where R is particle radius. With $Q = 818\,\mathrm{MW\,m^{-3}}$, and particle $\kappa \approx 44.8\,\mathrm{W\,m^{-1}\,K^{-1}}$, $\Delta T \approx 7.61 \times 10^{-5}\,\mathrm{K}$ in a 50 µm particle (conductivity is described in Appendix E).

In EBR-II, $\nabla T_{\text{avg}} = \Delta T / R > 10^5\,\mathrm{K\,m^{-1}}$. In 50 µm particles $\nabla T_{\text{avg}} \approx 2.5$ K/m. Although alloy migration was strongly driven in EBR-II fuel pins by Ludwig-Soret drift, within 50 µm particles Ludwig-Soret drift will be insignificant because ∇T is much smaller.

The time scale for Fickian diffusion to oppose Ludwig-Soret drift varies quadratically with the characteristic relaxation distance L as

$$\tau \approx \frac{L^2}{D_i} \tag{C.6}$$

The ratio of the characteristic relaxation times for 3.528 mm diameter EBR-II fuel slugs and 50 µm particles is 2.48×10^5. This means that as soon as Ludwig-Soret drift moves an atom within a particle, Fickian diffusion quickly pushes it back into its original position: Radial drift of alloy constituents observed in EBR-II fuel slugs is physically precluded in IMFR fuel particles [29, p. 92].

Appendix D. Fuel Alloy

D.1 TRU Isotope Mixture

Using TRU from fast reactors allows a lower TRU fraction because it contains less of the "neutron poison" isotopes (Np-237, Pu-242, Am-241) than would TRU from light-water reactors. Rather than absorbing thermal neutrons, these isotopes fission efficiently in a fast spectrum, and therefore do not accumulate. The isotope weight fractions in TRU from IMFR fuel were estimated by solving the Bateman equations using Maple [36]:

$$\frac{\mathrm{d}\mathbf{N}}{\mathrm{d}t} = (\mathbf{\Sigma}\,\varphi - \mathbf{A})\,\mathbf{N} \tag{D.1}$$

over a 100 year interval, where $\mathbf{N}$ is atom densities, $\mathbf{\Sigma}$ is cross sections, $\mathbf{A}$ is activities, and φ is neutron flux — not volume mixing ratio ϕ. The neutron flux φ and cross sections $\mathbf{\Sigma}$ were calculated by OpenMC using data from ENDF/B-VIII.0 [9]; evolution of φ and $\mathbf{\Sigma}$ were not modeled in Maple. The time derivative of the number of ^{238}U atoms was set equal to the negative of the sum of the time derivatives of TRU atoms, to simulate replacement of fissioned TRU by ^{238}U during fuel processing. This isn't quite right because ^{238}U does fission slightly in a fast spectrum, but the effect of including it should be small. The simulation was started with TRU estimates, then run until equilibrium. OpenMC was re-run with the final isotope mixture to calculate new values of $\mathbf{\Sigma}$ and φ, after which Maple was re-run, and produced the same equilibrium isotope mixture. The ratio of ^{239}Pu to total Pu remains within the 68%–71% range, which is not suitable for weapons proliferation [48, § 12.9]. TRU fractions used in OpenMC simulations are shown in Table D.1.

Table D.1: TRU Fractions

	Weight %	
Isotope	In LWR	In IMFR
^{241}Am	3	0.7
^{243}Am	2	1.0
^{244}Cm	1	1.1
^{237}Np	5	0.8
^{239}Np	≈ 0	0.2
^{238}Pu	2	0.6
^{239}Pu	47	65.8
^{240}Pu	23	25.1
^{241}Pu	11	3.1
^{242}Pu	7	1.8

Zirconium was not used to increase solidus temperature; rather it reduces U-238 concentration, thereby decreasing the breeding ratio. There are few data concerning the solidus temperature of alloys of uranium, transuranic elements, zirconium, and fission products. The plutonium fraction in TRU content is in the range 90 – 95%; the effect of minor TRU isotopes on solidus temperature is small. The Pu-U phase diagram [16, p. 1939] shows the solidus temperature of U-10Pu is about 1250 K — well above the sodium boiling temperature of 1154 K. Zirconium and most fission products that are soluble in uranium, such as molybdenum, increase solidus temperature. Many

fission products — especially alkali metals and alkaline earths — are not soluble in uranium and probably tend to depress solidus temperature. The solidus temperatures of fuels with 5% burnup are probably well above 1200 K.

D.2 Method of Alloy Fraction Calculation using OpenMC

Fuel alloy fractions were calculated by repeatedly using OpenMC to calculate the effective multiplication factor k_{eff} and the breeding ratio BR. To start the process, two guesses were made of the weight fractions of the combined set of transuranic isotopes (Tr_1 and Tr_2), and zirconium (Zr_1 and Zr_2). Results after n steps were analyzed using a least-squares method, similar to a Kalman filter, to fit the transuranic and zirconium fractions to planes:

$$\begin{aligned} \mathbf{W_k}\,\mathbf{A}\,\mathbf{a} &= \mathbf{W_k}\,\mathbf{k}_{\text{eff}} \\ \mathbf{W}_{\text{BR}}\,\mathbf{A}\,\mathbf{b} &= \mathbf{W}_{\text{BR}}\,\mathbf{BR}\,, \end{aligned} \tag{D.2}$$

where $\mathbf{W_k}$ and $\mathbf{W}_{\text{BR}}$ are matrices containing the inverses of the standard deviations computed by OpenMC for k_{eff} and BR on their diagonals, multiplied by a "forgetting weight" λ^{n-i} (with $\lambda = 0.6$ chosen), and $A[i,:] = [\text{Tr}_i, \text{Zr}_i, 1]$. The solutions for $\mathbf{a}$ and $\mathbf{b}$ are coefficients in least-squares plane equations for Tr and Zr:

$$\begin{aligned} a_{\text{Tr}}\,\text{Tr} + a_{\text{Zr}}\,\text{Zr} + a_0 &= k_{\text{eff}} \\ b_{\text{Tr}}\,\text{Tr} + b_{\text{Zr}}\,\text{Zr} + b_0 &= \text{BR}\,. \end{aligned} \tag{D.3}$$

These equations can be solved for new values of Tr and Zr by setting the right-hand sides equal to 1.0, the desired values. A faster method is a Newton iteration: Construct a first-order Taylor expansion, *viz.*

$$f(x_n) = f(x_{n-1}) + f'(x_{n-1})\,\delta x + \ldots, \tag{D.4}$$

where $\delta x = x_n - x_{n-1}$. By setting $f(x_n) = 0$, one obtains the Newton iteration

$$f'(x_{n-1})\,\delta x = -f(x_{n-1}) \text{ , or } \mathbf{J}\,\delta\mathbf{x} = -\mathbf{F}(x_{n-1}) \tag{D.5}$$

in the multivariate case, where $\mathbf{J}$ is the Jacobian obtained from Equation (D.3)

$$\begin{bmatrix} a_{\text{Tr}} & a_{\text{Zr}} \\ b_{\text{Tr}} & b_{\text{Zr}} \end{bmatrix} = \begin{bmatrix} \frac{\partial k_{\text{eff}}}{\partial \text{Tr}} & \frac{\partial k_{\text{eff}}}{\partial \text{Zr}} \\ \frac{\partial \text{BR}}{\partial \text{Tr}} & \frac{\partial \text{BR}}{\partial \text{Zr}} \end{bmatrix}, \tag{D.6}$$

$\mathbf{x} = [\text{Tr}, \text{Zr}]^T$ represents the weight fractions of the combined set of transuranic isotopes and zirconium, and $\mathbf{F}(x_{n-1}) = [\mathbf{k}_{\text{eff}_{\mathbf{n-1}}} - 1, \mathbf{BR}_{n-1} - 1]^T$. k_{eff} and BR are not different by orders of magnitude, so column scaling is not necessary to minimize the condition number κ_1. A "wrapper" program executed OpenMC, which does not calculate a Jacobian, in a Newton iteration. Using a least-squares method with a Kalman filter-like "forgetting weight" expresses the assertions "the Jacobian becomes more accurate as the solution is approached" and "the problem becomes locally linear as the solution is approached."

Appendix E. Fuel Thermal Conductivity

E.1 Sodium Conductivity

The thermal conductivity of Sodium [21, § 2.1] is

$$\kappa = 124.67 - 0.11381\,T + 5.5226 \times 10^{-5}\,T^2 - 1.1842 \times 10^{-8}\,T^3$$

At $T = 900\,\mathrm{K}$, $\kappa_{\mathrm{Na}} = 58.37\,\mathrm{W\,m^{-1}\,K^{-1}}$

E.2 Billone/DiMelfi/Hofman Correlation for Alloy Fuels

The linear approximation to the quadratic Billone/DiMelfi/Hofman correlation [2, 28, 15] for thermal conductivity of solid U-Pu-Zr-Mo-Fs fuels, which is valid below $\approx 1000\,\mathrm{K}$, is

$$\begin{aligned} \kappa &= 17.5 + 0.0245\,T + C_{\mathrm{Mo}}\,C_{\mathrm{Pu}}\,C_{\mathrm{Zr}}\,e^{-0.15\,Fs}, \text{ where} \\ C_{\mathrm{Mo}} &= (1.0 - 1.45\,Mo)\,, \\ C_{\mathrm{Pu}} &= (1.0 - 1.25\,Pu)\,, \\ C_{\mathrm{Zr}} &= (1.0 - 2.33\,(Zr + 0.0607\,Bu))\,, \end{aligned} \tag{E.1}$$

Zr, Mo, Pu, and Fs are weight fractions. "Fs" means "fissium," but in this case refers to the metallic surrogate composed only of a mixture of noble metal fission products, mostly molybdenum, palladium, and ruthenium, resulting from pyrometallurgical processing at EBR-II, not all fission products as in Table I.6. "Bu" means burnup and appears in the zirconium fraction because 5.16% of fission product metals are zirconium. The exponential factor does not account for it because zirconium did not appear in the "fissium" alloy resulting from pyrometallurgical processing at EBR-II. After gases escape, zirconium composes 6.07% of fission products (see Table H.1).

Non-noble fission products are generally not miscible in actinides. They form crystal structure defects and intermetallic compounds, both of which are scattering centers. To account for this, the author added an $\alpha\,Bu$ term to the exponential. Using data from Table H.1, $Fs \approx 0.44\,Bu$, and Equation (E.1) becomes

$$\kappa = 17.5 + 0.0245\,T + C_{\mathrm{Mo}}\,C_{\mathrm{Pu}}\,C_{\mathrm{Zr}}\,e^{-(\alpha + 0.066)\,Bu} \tag{E.2}$$

E.3 Bruggeman Model

The Bruggeman model for thermal conductivity of a porous medium [10] is.

$$\phi\left(\frac{\kappa_f - \kappa_{\mathrm{eff}}}{\kappa_f + 2\kappa_{\mathrm{eff}}}\right) + (1-\phi)\left(\frac{\kappa_{Na} - \kappa_{\mathrm{eff}}}{\kappa_{Na} + 2\kappa_{\mathrm{eff}}}\right) = 0 \tag{E.3}$$

where κ_f is the conductivity of solid fuel, κ_{Na} is the conductivity of sodium, and κ_{eff} is the conductivity of the medium.

The Bruggeman model is used twice, first for porous (or solid) particles and then for particles in paste with $\phi_{\text{paste}} \approx 78\%$. The results are shown in Table E.1.

Table E.1: Thermal Conductivities κ ($\mathrm{W\,m^{-1}\,K^{-1}}$) at $T = 955\,\mathrm{K}$

Burnup		$\alpha = 3$			$\alpha = 6$		
Fraction	ϕ_{particle}	Alloy	Particle	Paste	Alloy	Particle	Paste
0%	100%	41.72	41.72	44.56	41.72	41.72	44.56
5%	75%	41.60	44.86	47.11	41.53	44.81	47.07
7.1%	75%	41.55	44.83	47.08	41.46	44.76	47.03

The results in Table I.4 were computed with $\alpha = 3$. Using $\alpha = 6$ increases calculated temperatures about 1.2 K at 5% burnup.

The increase in conductivity compared to solid alloy is about 8% at 2% burnup ($\phi_{\text{particle}} = 0.75$), and about 13% for particles in paste. These ratios are nearly insensitive to burnup or α (less than 0.1% change).

The Bruggeman model cannot be used simply as if the particles and paste were a single porous medium with $\phi \approx 0.58$ because it is not linear, and therefore superposition does not apply. Superposition significantly over estimates conductivity, $\approx 47.26\,\mathrm{W\,m^{-1}\,K^{-1}}$

Appendix F. Thermal Safety Calculation

Values of reactivity ρ and worth $\rho(\$)$ were calculated for $0 < \Delta H < 20\,\mathrm{mm}$. Delayed neutron activity was, as expected, nearly constant with $\beta_{\text{eff}} = 0.00370 \pm 9{\times}10^{-5}$ (variations are attributed to the stochastic nature of Monte Carlo simulation). The relationship between expansion and worth was analyzed using least-squares fits to linear and quadratic polynomials. The average difference between the polynomials was 0.6% of the standard deviation of the least-squares estimates so $\rho(\$)$ was calculated as the derivative of the linear estimate:

$$\frac{\partial \rho(\$)}{\partial H} = -5.56\,\mathrm{¢\,mm^{-1}}\,. \tag{F.1}$$

With ρ_{metal} in Equation (F.2) being density, not reactivity, using

$$\begin{aligned} \rho_{\mathrm{U}} &= 19.36 - 1.03347 \times 10^{-3}\,T \\ \rho_{\mathrm{Pu}} &= 17.13 - 1.01 \times 10^{-3}\,T \\ \rho_{\mathrm{Zr}} &= 6.577 - 1.83 \times 10^{-4}\,T\,, \end{aligned} \tag{F.2}$$

from which, using the composite density formula

$$\frac{1}{\rho_{\text{composite}}} = \sum_i \frac{w_i}{\rho_i} \text{ and } \frac{\partial \rho_{\text{composite}}}{\partial T} = \rho^2_{\text{composite}} \sum_i \frac{w_i}{\rho_i^2} \frac{\partial \rho_i}{\partial T}\,, \tag{F.3}$$

wherein w_i are weight fractions, giving

$$\frac{\partial \rho}{\partial T} = -8.2 \times 10^{-5}\ \mathrm{K}^{-1}\,. \tag{F.4}$$

Because fuel paste is contained laterally and can therefore expand only axially, for the entire fuel region, $\frac{\partial H}{\partial T} = -H\frac{\partial \rho}{\partial T} = 0.13\,\mathrm{mm\,K^{-1}}$. Therefore

$$\frac{\partial \rho(\$)}{\partial T} = \frac{\partial \rho(\$)}{\partial H}\,\frac{\partial H}{\partial T} = -0.73\,¢\,K^{-1}. \tag{F.5}$$

This is a conservative estimate because expansion of other metals in the fuel alloy was not included, that is, $\frac{\partial \rho}{\partial T} > 8.2 \times 10^{-5}\,\mathrm{K}^{-1}$.

Using Equation (F.4), for fuel to expand 22 mm, that is, to completely occupy the plenum, the temperature must increase $22/0.13 = 169\,\mathrm{K}$. With a normal operating temperature of $\approx 930\,\mathrm{K}$, this increase to 1099 K is well below the 1154 K boiling temperature of sodium. A further increase to 1154 K would force 7.2 mm of "quiet zone" sodium into the gas management system. The gas management system contains an external rupture diaphragm to prevent this expansion from rupturing fuel elements.

Appendix G. Resonant Frequency Calculation

The Rayleigh-Ritz method is used to calculate the fundamental resonant frequencies of elements rigidly connected to the grid plate:

$$\omega^2 = \frac{V}{T^*}\,, \tag{G.1}$$

where

$$\begin{aligned} V &= \sum_{i=1}^{n} E_i\, I_i \int_{z_{i-1}}^{z_i} \mathrm{d}z \frac{\mathrm{d}^2 w(z)}{\mathrm{d}z^2}\,, \\ T^* &= \sum_{i=1}^{n} m_i \int_{z_{i-1}}^{z_i} \mathrm{d}z\, w(z)^2\,, \end{aligned} \tag{G.2}$$

E_i is the effective Young's modulus ($233 - 0.0558\,T$ GPa $\approx$ 194 GPa for RAFM steel at 700 K, estimated $\approx$233 GPa for the shield, zero for fuel paste because it is a Bingham plastic, not a rigid body, zero for sodium and argon), I_i is the moment of inertia, m_i is the mass linear density $\mathrm{kg\,m^{-1}}$, and the trial function for a cantilever supported at one end is

$$w(z) = z_r^2(z_r^2 - 4z_r + 6) \text{ where } z_r = \frac{z}{L}\,. \tag{G.3}$$

In fuel elements, the bottom shield, fuel region, quiet zone, and plenum are modeled as separate regions because they have different mass and stiffness. Control and shield elements have only one zone. The "squeeze film" effect of $\approx$9.6 mm sodium surrounding each element was included in the calculation by adding $\left(1 + 2\,\frac{A_{\text{element}}}{\text{gap}\cdot\text{perimeter}}\right)\rho_{\mathrm{Na}} A_{\text{element}}$ to the structure's linear mass density.

The Rayleigh-Ritz method approximates the eigenvalues of the Euler-Bernoulli beam equation

$$E(x)\,I(x)\,\frac{\partial^4 w(x,t)}{\partial x^4} + \eta\,I(x)\,\frac{\partial^5 w(x,t)}{\partial x^4\,\partial t} + \rho\,A\,\frac{\partial^2 w(x,t)}{\partial t^2} + c_{\text{eff}}\frac{\partial\, w(x,t)}{\partial t} = 0\,, \tag{G.4}$$

where $w(x,t)$ is transverse deflection, η is internal viscosity, and c_{eff} is defined in Table G.1.

Equation (G.4) has complex eigenvalues if $\eta \neq 0$. Quantities defined in Table G.1 are approximations used to account for viscosity. Values are shown in Table G.2.

Table G.1: Seismic-relevant Quantities

Name	Formula
Hydrodynamic Damping	$c_{\text{eff}} = \frac{3}{2}\,\pi\,\eta_{\text{Na}}\left(\frac{L}{\text{gap}}\right)^3$
Chen-Sandberg Correlation	$\zeta = \frac{c_{\text{eff}}}{2\sqrt{K\,m_{\text{eff}}}}$
Structural Stiffness	$K = 3\,\frac{E\,I}{L^3}$
Effective Mass	$m_{\text{eff}} = m + \pi\,\chi\,\rho_{\text{Na}}\,A$
Virtual Mass Coefficient	$\chi = \frac{\left(\frac{P}{D}\right)^2+1}{\left(\frac{P}{D}\right)^2-1}\ 1.64$
Frequency Response Function	$H(\beta) - 1 = \frac{1}{\sqrt{(1-\beta^2)^2+4(\zeta\,\beta)^2}}$
Seismic Frequency Ratio	$\beta = \frac{f_{\text{seismic}}}{f_{\text{element}}}$
Seismic Force	$F_{\text{seismic}} = m\,a_{\text{seismic}}$
Deflection at resonance	$\delta_{\text{peak}} = \frac{F_{\text{seismic}}}{2\,K\,\zeta}$
Deflection off resonance	$\delta = \frac{F_{\text{seismic}}\,H(\beta)}{K}$

P is pitch; D is hydraulic diameter of one fuel element.
A and m are the area and mass of one element.
η_{Na} is sodium viscosity at 700 K. ρ_{Na} is sodium density at 700 K

The frequency response function $H(\beta)$ accounts for the non-conservative linear damping and fifth-order Kelvin-Voigt resonance terms in Equation (G.4). Applying the Chen-Sandberg correlation ($\zeta \propto H(\beta)^{-1}$), a first-order nondimensional damping ratio, is an approximation of the effect of external viscosity projected onto $w(z)$, that reduces the resonant frequency for fuel elements by $\sqrt{1-\zeta^2}$ [14, 13].

Table G.2: Seismic-relevant Quantity Values

Quantity	Value					
χ	0.104					
c_{eff} (Pa·s)	1.64 Pa·s					
m_{eff} (kg)	33.5 kg					
	Fuel element		Shield element		Control element	
K (N/m)	3.77×10^6		3.10×10^6		2.22×10^5	
ζ	0.104		0.122		1.741	
	Free	Damped	Free	Damped	Free	Damped

(Cont.)

(Continued from previous page)

Quantity	Value					
f (hz)	82.1	81.6	115.4	114.6	43.7	Overdamped
f_{seismic}	0.5	30	0.5	30	0.5	30
β	6.09×10^{-3}	0.365	4.33×10^{-3}	0.256	1.14×10^{-2}	0.686
$H(\beta)-1$	3.63×10^{-5}	0.150	1.82×10^{-5}	0.070	-2.30×10^{-4}	-0.410
a_{seismic} (g)	0.3	0.5	0.3	0.5	0.3	0.5
F_{seismic} (N)	83.373	138.96	1224.1	2040.2	184.22	307.04
δ_{peak} (% of gap)	1.86	3.10	1.72	2.87	Overdamped	
δ (% of gap)	0.389	0.744	0.421	0.751	0.884	0.869

The resonant frequencies are all well above the 0.5-30 Hz frequency of most earthquake motions. $\zeta > 1$ and $H(\beta) < 0$ for control elements indicate that they do not vibrate because they are overdamped. The deflections δ_{peak} and δ are approximate upper bounds of solutions of Equation (G.4) that show that viscosity provides internal hysteretic damping that broadens resonance peaks. Deflections $< 1\%$ of the gap between elements demonstrates the "squeeze film" approximation is valid. A total-core frequency analysis as part of detailed design is expected to confirm this.

Appendix H. Fission Products and Process Details

This appendix provides supporting details for the fuel processing system described in Part II, including full fission product tables and stage-by-stage partitioning data.

Table H.1 shows a detailed list of fission products, the intermetallic compounds formed among fission products, and the intermetallic compounds formed between fission products and cadmium. The amounts are based on data from ENDF/B-VIII.0 [9]. Trace fission products — beryllium, carbon, niobium, thulium, tritium — and magnesium transmuted from sodium, are not included in this analysis.

Table H.1: Fast Reactor Fission Products and Physical Separation

Element	**Weight***	**Weight Percent**	**Mole Percent**	**Radiotoxicity Sv/MWe-yr**	**Half Life**†	**Intermetallic Compounds**
Antimony	381 mg	0.04	0.03	886	2.759 y	↓ Zr_3Sb
Arsenic	0.82 mg	0.00	0.00			↓ Zr_3As
Barium	29.83 g	2.95	2.32			↓ $BaBr_2, BaI_2, BaCd_{11}$
Beryllium	0.124 μg	0.00	0.00	9.814×10^{-8}	1.600 My	↓ Metallic Fine
Bromine	312 mg	0.03	0.04			↓ $BaBr_2$
Cadmium	4.152 g	0.41	0.39	1070	14.10 y	Solvent Phase
Caesium	68.32 g	6.76	5.49	1.254×10^{6}	30.04 y	↑ Elemental Vapor
Carbon	1.15 μg	0.00	0.00	1.100×10^{-6}	5700 y	↓ Graphite Soot
Cerium	65.23 g	6.46	4.97	613.1	285.0 d	↓ $CeCd_{11}$
Dysprosium	420 mg	0.04	0.03			↓ $DyCd_{11}$
Erbium	35.12 mg	0.00	0.00			↓ $ErCd_{11}$
Europium	1.521 g	0.15	0.11	4.068×10^{3}	8.593 y	↓ $EuCd_{11}$
Gadolinium	4.862 g	0.48	0.33	1.482×10^{-4}	240.0 d	↓ $GdCd_{11}$
Gallium	0.41 μg	0.00	0.00			↓ Zr_5Ga_3
Germanium	1.12 mg	0.00	0.00			↓ Zr_5Ge_3
Holmium	62.14 mg	0.01	0.00	1.001×10^{-1}	1200 y	↓ $HoCd_{11}$
Indium	510 mg	0.05	0.05	3.506×10^{-9}	441 Ty	↓ $InPd$

(Cont.)

(Continued from previous page) Element	Weight*	Weight Percent	Mole Percent	Radiotoxicity Sv/MWe-yr	Half Life†	Intermetallic Compounds
Iodine	8.112 g	0.80	0.68	4.457	16.10 My	↓ BaI_2
Lanthanum	32.14 g	3.18	2.47	1.037×10^{-10}	102.0 Gy	↓ $LaCd_{11}$
Magnesium ‡	≈10 mg	—	—			Soluble
Molybdenum	141.6 g	14.02	15.77			↓ Metallic Sinker
Neodymium	138.2 g	13.68	10.23			↓ $NdCd_{11}$
Niobium	814.2 μg	0.00	0.00	6.035×10^{-1}	16.13 y	↓ Metallic Sinker
Palladium	98.42 g	9.74	9.88	1.062×10^{-2}	6.500 My	Soluble
Praseodymium	31.02 g	3.07	2.35	5.987	17.28 m	↓ $PrCd_{11}$
Promethium	1.121 g	0.11	0.08	1.001×10^{4}	5.531 y	↓ $PmCd_{11}$
Rhodium	36.14 g	3.58	3.75	4.475×10^{-1}	2.902 y	↓ $ZrRh_3$
Rubidium	4.12 g	0.41	0.51	1.381×10^{-5}	48.10 Gy	↑ Elemental Vapor
Ruthenium	134.8 g	13.35	14.25	7812	1.020 y	↓ $ZrRu$
Samarium	24.12 g	2.39	1.71	3.789	90.0 y	↓ $SmCd_{11}$
Selenium	412 mg	0.04	0.06	0.322	337.0 ky	↓ $ZrSe$
Silver	7.821 g	0.77	0.77	2.056	249.8 d	↓ $AgCd_3$
Strontium	11.14 g	1.10	1.36	8.532×10^{5}	28.79 y	↓ $SrCd_{11}$
Technetium	35.12 g	3.48	3.83	14.11	214.0 ky	↓ Metallic Sinker
Tellurium	18.92 g	1.87	1.58	329.8	57.40 d	↓ $ZrTe$
Terbium	421 mg	0.04	0.03	6.481×10^{-12}	72.30 d	↓ $TbCd_{11}$
Thulium	12.14 μg	0.00	0.00	2.768×10^{-5}		↓ $TmCd_{11}$
Tin	6.812 g	0.67	0.61	10.41	230.0 ky	↓ Cd_3Sn, Zr_5Sn_3
Ytterbium	4.12 μg	0.00	0.00			↓ $YbCd_6$
Yttrium	6.14 g	0.61	0.74	7.598×10^{4}	2.671 d	↓ YCd_6
Zirconium	52.14 g	5.16	6.11	1.048	1.530 My	↓ $ZrCd_2$
Gases						
Krypton	3.82 g	0.38	0.49		10.75 y	Off-gas
Xenon	148.1 g	14.66	12.04		36.40 d	Off-gas
Total	1010 g	100.00	100.00	2.19×10^{6}		

* Per megawatt-electric year

† Half life of the isotope that produces the greatest total radiotoxicity

‡ Magnesium arises from activation of sodium, not as a fission product

The 10% bleed from within fuel elements results in ≈240 liters per hour of ≈7.8% slurry flowing from the reactor to the processor. If every particle in ≈7.8% slurry from the reactor were processed, 1% of the total inventory would be processed every fifty hours (≈80 kg d^{-1}), and average particle residence in the reactor would be ≈400 days. This would impose an unnecessary processing load and undesirably tilt the plutonium inventory toward ^{239}Pu. Reducing the flow rate from the reactor risks sedimentation in the transfer lines, so only a fraction of arriving slurry is processed.

If only particles that have remained in the reactor for several years before being processed were selected, to achieve a specified burnup, the process would oscillate with a period of several years by selecting no particles at the beginning, all particles after several years, then no particles again.

Instead of selecting particles using a criterion such as density, which would be a complicated process, if it can be done at all, a fraction is withdrawn continuously. The 840 MWth reactor consumes ≈310 kg of fuel — almost exclusively plutonium and other TRU — per year, nearly one kilogram per day; to simplify discussion, assume one kilogram per day. To maintain a fission product fraction of 5% it is necessary to process ≈20 kg d^{-1} of fuel, ≈14 g min^{-1} of fuel particles. Fresh fuel particles have a density of ≈17 g cm^{-3} and 1.6% burnup fuel particles have a density of 10.4 g cm^{-3} (which doesn't change much after 1.6% burnup). Assuming average particle burnup >1.6%, it is necessary to process ≈2.4 L d^{-1} of fuel, ≈31 L d^{-1} of ≈7.8% slurry, or ≈21 cm^3 min^{-1} of slurry containing ≈1.6 cm^3 min^{-1}.

At the beginning of operation the fuel would contain no fission products. One way to reach the 5%

burnup goal is to postpone starting fuel processing until the fuel reaches that state. Another is to begin processing immediately, after which burnup would asymptotically approach the desired level. A hybrid possibility is to start slowly and accelerate to the calculated rate when average burnup approaches the desired level.

H.1 Dissolving Fuel Particles

The argon and particle underflow from the separation cascade is sparged near mid level into a 1000 K cadmium hydrocyclone, slightly inwardly from tangentially, to mix them into the bulk using Dean vortices, giving them a chance to dissolve instead of sliding down to the underflow.

Tangential injection of the high-temperature particle aerosol creates bubbles and establishes a central gaseous vortex core that acts as a stripping manifold. In addition to the particle aerosol entering tangentially, the vortex is enhanced by a rotating magnetic field, and tangential injection of cadmium and argon vapor reflux from later stages. The 50 µm fuel particles dissolve quickly, releasing fission product metals, and krypton and xenon that did not escape during operation. The high velocity and turbulence of the hydrocyclone facilitate rapid diffusion of alkali metal vapors and fission gases into the argon carrier gas, and centrifugal ejection of insoluble noble metals to the periphery.

Noble metals sink in the 1000 K stage because their densities are greater than liquid cadmium. Intermetallic compounds with zirconium are listed but might not form if residence in the 1000 K stage is short. There is a sweet spot, best determined by experiments, between removing pure noble metals, perhaps incompletely (short residence), and removing them completely, partly as zirconium compounds (long residence). The hydrocyclone underflow is concentrated by a diafilter, with the permeate proceeding to the next stage. Concentrated solids are washed with clean cadmium in a continuous-flow counter-current wash column, with the wash effluent returning to the vortex. The washed concentrate enters a 900 K argon nebulizer that strips the cadmium into the gas phase. Particles are separated by a cyclone. Argon and cadmium vapors are sparged tangentially into the 1000 K hydrocyclone to assist the vortex.

Some of the noble metals have high value, as shown in Table H.2. It might be necessary to store rhodium and ruthenium, separately year by year, for ten half lives before they can be sold, and the paperwork to sell them might eliminate the possibility of profit. Technetium powder could, in principle, be transmuted to more valuable ruthenium and rhodium in a thermal neutron flux. Careful analysis and perhaps experiments would be necessary to determine whether such a project would be a profit or loss center.

Table H.2: Fission Product Noble Metal Recovery

Element	**Amount kg/yr**	**Density g cm^{-3}**	**Value $/gram**	**Value $/yr**	**$t_{1/2}$ years**
Technetium	14.0	11.0	???	???	214 thousand
Pd	39.4	12.02	$40	$1,576,000	6.5 million
$ZrPd_3$	50.66	10.9	$23	$1,165,180	6.5 million
Rh	14.5	12.41	$257	$3,527,300	2.902
$ZrRh_3$	18.78	10.8	$195	$2,925,000	2.902
Molybdenum	56.6	10.28	—	—	∞

(Cont.)

(Cont.) **Element**	**Amount kg/yr**	**Density g cm^{-3}**	**Value $/gram**	**Value $/yr**	**$t_{1/2}$ years**
Ru*	53.9	12.45	$49	$2,548,000	1.020
ZrRu	102.6	9.2	???	???	1.020
Cd		7.48		Solvent	

*Despite the strong zirconium-ruthenium bond, a small amount of elemental ruthenium might appear

Intermetallic compounds formed in the 1000 K stage are shown in Table H.3. Silver particles appear in molten sodium. Silver does not form a sodium intermetallic compound, but its zirconium intermetallic compounds have very high melting points. Barium halides and all other metals remain in solution at 1000 K.[2] These compounds, which would only form if residence in the 1000 K stage is long enough, are shown in Table H.3.

Table H.3: Sodium Intermetallic Compounds

Element	**Sodium Precursor**	**Displacement Product**	**Density** g cm^{-3}
Antimony	Na_3Sb	Zr_5Sb_3	6.83
Arsenic	Na_3As	Zr_3As	6.28
Bromine	NaBr	$BaBr_2$	4.47
Gallium	$NaGa_4$	Zr_5Ga_3	6.54
Germanium	NaGe	Zr_5Ge_3	6.54
Iodine	NaI	BaI_2	4.47
Selenium	Na_2Se	ZrSe	6.42
Silver	—	$AgZr_2$	6.60
Silver	—	AgZr	7.15
Tellurium	Na_2Te	ZrTe	6.31
Cd		Solvent	7.48
Tin	NaSn	Zr_xSn_y	7.6–7.8

Particles that float in the 1000 K stage are removed from the vortex by a weir at the top of the cadmium hydrocyclone, then concentrated, washed, and cadmium is separated in the same way as for noble metal particles. Unlike cadmium intermetallic compounds, they are extremely difficult to dissociate. Some of the zirconium stannides are more dense than cadmium, and might harmlessly appear with the noble metal underflow.

H.2 Separating Fission Products from Unused Fuel

The contents of the 800 K stage are shown in Table H.4. Some barium, strontium, and yttrium re-dissolve, but reach equilibrium concentrations in the reflux system rather than accumulating. Barium halides do not dissociate or dissolve at 800 K.

[2]Barium halides have varying solubility depending upon temperature; some crystals appear at all stages.

Table H.4: 800 K Stage

Intermetallic Compound	**Physical Form**	**Density** ($\mathrm{g\,cm^{-3}}$)	
		Intermetallic	**Element**
$NpZr_2$	Solid Sink	10.9	20.25
$PuZr_2$	Solid Sink	10.2	15.4
$ZrCd_2$	Solid Sink	8.3	6.52
$BaCd_{11}$	Solid Suspension	7.5	3.51
Cd	Solvent	7.48	7.48
YCd_6	Solid Float	4.62	4.47
BaI_2	Solid Float	4.47	4.47
$BaBr_2$	Solid Float	4.47	4.47
$SrCd_{11}$	Solid Float	2.64	2.64

The contents of the 775 K lanthanide stage are shown in Table H.5. Particles are washed and dried in the same way as in the 800 K stage, but at 775 K. Barium halides that have not crystallized at higher temperatures are separated from the argon aerosol by their lower density.

Table H.5: 775 K Stage

Intermetallic Compound	**Physical Form**	**Density** ($\mathrm{g\,cm^{-3}}$)	
		Intermetallic	**Element**
$NpZr_2$	Solid Sink	10.9	20.25
$PuZr_2$	Solid Sink	10.2	15.4
$ErCd_{11}$	Solid Sink	8.45	9.07
$HoCd_{11}$	Solid Sink	8.35	8.79
$TbCd_{11}$	Solid Sink	8.28	8.23
$YbCd_6$	Solid Sink	8.22	6.90
$PmCd_2$	Solid Sink	8.18	7.26
Cd	Solvent	7.80	7.80
$DyCd_{11}$	Solid Float	7.72	8.55
$GdCd_{11}$	Solid Float	7.64	7.90
$SmCd_{11}$	Solid Float	7.59	7.52
$PmCd_{11}$	Solid Float	7.55	7.26
$NdCd_{11}$	Solid Float	7.51	7.01
$YbCd_{11}$	Solid Float	7.35	6.90
$CeCd_{11}$	Solid Float	7.45	6.77
$PrCd_{11}$	Solid Float	7.48	6.77
$LaCd_{11}$	Solid Float	7.42	6.16
$EuCd_{11}$	Solid Float	7.41	5.24
BaI_2	Solid Float	4.47	4.47
$BaBr_2$	Solid Float	4.47	4.47

At the 800 K and 775 K stages, to ensure the recovery of valuable transuranic species such as neptunium and plutonium, which might have made their way to the top of a column as low density $NpZr_2$ and $PuZr_2$, the process incorporates a closed-loop recycle path. By refluxing the light-fraction permeate to the 1000 K primary dissolution stage, any misplaced TRU compounds or actinide-bearing

crystals are re-dissolved, allowing for subsequent partitioning into the dense underflow in the correct stage. This reprocessing loop is intended to ensure that lanthanide waste streams remain well below the 1 ppm TRU threshold, with a secondary, much smaller, modular cascade a contingent possibility if lattice entrapment within the lanthanide-cadmium matrix is not ameliorated by this reflux.

The contents of the 765 K stage are shown in Table H.6. Transuranic-cadmium intermetallics crystallize and sink, leaving uranium, palladium, and zirconium in solution. Care must be taken to maintain the temperature above the peritectic point of uranium (746 K) to prevent forming UCd_{11} and $ZrCd_x$ crystalline precipitates. Transuranic-cadmium crystals are separated and washed, in the same way as in the 800 K stage, but at a lower temperature, to avoid re-dissolving them, then dried. Barium halides are removed from the top and processed as in higher-temperature stages. Zirconium-actinide intermetallic compounds are not troublesome because zirconium is needed in the alloy.

Table H.6: 765 K Stage

Intermetallic Compound	**Physical Form**	**Density** ($g\,cm^{-3}$)	
		Intermetallic	**Element**
$NpZr_2^*$	Solid Sink	10.9	20.25
$PuZr_2^*$	Solid Sink	10.8	19.84
$PuCd_{11}$	Solid Sink	9.12	19.84
$PaCd_{11}$	Solid Sink	9.05	15.37
$AmCd_{11}$	Solid Sink	8.94	13.67
$CmCd_{11}$	Solid Sink	8.96	13.51
$ThCd_{11}$	Solid Sink	9.01	11.72
Cd	Solvent	7.94	7.94
BaI_2	Solid Float	4.47	4.47
$BaBr_2$	Solid Float	4.47	4.47

*$NpZr_2$ and $PuZr_2$ do not dissociate.

Zirconium-cadmium intermetallic compounds shown in Table H.7 form in the 600 K stage. Uranium does not crystallize uniformly as cadmium is cooled to 600 K. Care must be taken to maintain the solution temperature above the cadmium melting point of 594 K. Uranium stubbornly remains in solution [16, p. 696], but with a concentration of only ≈ 0.02 at%. Uranium and part of the zirconium are separated from the underflow, while zirconium is also separated from the overflow, entering the same inter-stage diafilter. They are not washed because that would re-dissolve them. The solids are dried, cadmium dissociated, and the metals separated one from another by a 900 K argon nebulizer.

Table H.7: 600 K Stage

Intermetallic Compound	**Physical Form**	**Density** ($g\,cm^{-3}$)	
		Intermetallic	**Element**
U	Solute	19.05	19.05
Pd	Solute	12.02	12.02
UCd_{11}	Slush	9.05	19.05

(Cont.)

(Continued from previous page)

Intermetallic Compound	Physical Form	Density ($g\,cm^{-3}$)	
		Intermetallic	Element
Cd	Solvent	7.94	7.94
$ZrCd_z$	Solid Suspension	7.7–8.4	6.5
In	Solute	6.97	6.97

The final permeate shown in Table H.8 is a solution of cadmium, indium, and palladium, with uranium at ≈ 0.02 at% in cadmium. Palladium-sodium intermetallics are formed with residual sodium not initially removed, and by adding sodium; some float and some sink. If excess sodium had remained at the first stage, these compounds might have precipitated at higher temperatures. Precipitates are removed from both the overflow and underflow, then concentrated and washed with cadmium using diafilters, as in the 800 K stage. Palladium is separated from cadmium and sodium using a 1200 K argon nebulizer.

Table H.8: Final Permeate

Intermetallic Compound	Physical Form	Density ($g\,cm^{-3}$)	
		Intermetallic	Element
U	Solute	19.05	19.05
$NaPd_3$	Solid Sink	8.3	12.02
Cd	Solvent	7.94	7.94
In	Solute	6.97	6.97
NaPd	Solid Float	6.1	12.02

While this monograph focuses on the integral fuel cycle required for autonomous IMFR operation, the underlying processing technology is inherently scalable. Future expansions, subject to regulatory framework adjustments, could allow for the transition from an integral closed-loop system to a regional fuel-recycling service.

Appendix I. Future Work

I.1 Fuel Circulation

All surfaces, including eductors, receive a $>10\,\mu m$ coating of W-10Ta using chemical vapor deposition to withstand forty years of abrasion. Experiments using actual fuel or a simulant paste containing particles composed of depleted uranium and zirconium, without transuranics, are necessary to verify that this is sufficient.

If fuel is deposited only near the center of a fuel element by each spoke of the return web, a moat and rampart might form around the orifice. The rampart might periodically collapse into the moat, leading to "hiccups" or "chugging" in the circulation system. Whether that occurs is impossible to determine *a priori* because Bingham plastic behavior is very strongly and nonlinearly dependent upon yield stress, and Bingham paste viscosity, which is different from dynamic viscosity that can be computed by the Krieger-Dougherty equation for low-density slurry. There are no data concerning these parameters in a $\approx 78\%$ paste of actinide fuel particles in sodium. Even if these data were

available, the combination of steady-state Navier-Stokes equations and the sedimentation equation is a stiff system, for which it might be difficult to produce meaningful solutions. If "hiccups" or "chugging" occur in experimental apparatus, the horizontal transport web will need several radial orifices instead of one. Determining their geometry and spacing will require experiments.

Because a Bingham plastic of actinide particles in sodium has not been studied in a laboratory and is difficult to examine computationally, it will be necessary to verify that $\approx 78\%$ paste entering the 6 mm eductor orifice can be broken into a slurry, or remains in a "jammed" state. For the same reason, it will be necessary to verify that expected rheological stability due to high viscosity prevents "chugging."

When the reactor is not operating and fuel is not circulating, upcomer channels will fill with $\approx 78\%$ paste instead of $\approx 7.8\%$ slurry. The eductor pressure necessary to clear that slug is much greater than the pressure necessary to maintain flow of $\approx 7.8\%$ slurry. For the same reasons mentioned above, this pressure is difficult or impossible to compute *a priori*; experiments will be required.

There are several ways to start circulation, each with their own advantages and hazards. Experiments will be necessary to choose the best method.

- The "brute force" method of modulating the eductor motive sodium pump power during the transition from startup to an equilibrium operational state requires a sufficiently strong eductor and upcomer assembly, and sufficiently powerful motive sodium pumps.
- Fabricate a motive sodium channel parallel to the upcomer. Produce periodic longitudinal perforations, $\lesssim 10\,\mu$m diameter, angled upward at 20-30°. When the upcomer is initially filled with $\approx 78\%$ paste, the topmost perforation will liquefy and transport some fuel, reducing the weight above the next one, until the $\approx 7.8\%$ slurry is formed. In the limit of increasing the number and decreasing the spacing, this becomes a porous boundary with holes drilled by lasers.
- A scheme similar to the previous one, but with the parallel channel connected to one of the gas control lumens; this would require horizontal channels in five of the walls to connect to all six upcomers, leaving two channels for fission-gas management (Section I.1.7). The advantage of this scheme is that it does not increase the downcomer sodium load.
- Abandon an eductor for forming circulation within each fuel element, in favor of one of the previous two schemes. Eductors to transport fuel to the processor are still required. They might have the same "startup slug" problem, and it might be difficult to find a place for them outside fuel elements.

I.2 Parametric Studies

As was observed in Table I.4, with the fuel paste fraction held constant, maximum fuel temperatures increased quadratically as the number of coolant tubes decreased, even though the coolant fraction increased linearly. Several parameters are related. Rather than holding fuel paste fraction constant, the fuel paste fraction can be computed as a function of a specified maximum temperature for different numbers of coolant tubes. If the fuel paste VMR is held constant at $\approx 78\%$, the fuel alloy volume fraction will depend upon the volume fractions of fuel paste, coolant, and structure. The results of a brief thermal-only study conducted for four coolant tube densities are shown in Table

I.1. A Monte Carlo study was not undertaken to compute fuel alloy fissionable requirements, or whether the thermal power density used in the study, 818 kW m^{-3}, could be achieved.

Table I.1: Tube Parameter Study for $T_{\max} \approx 838$ K

Number of Tubes		Tube	Fractions		
Per Edge	Total	Width	Paste	Structure	Coolant
10	271	3.1250	0.6762	0.2136	0.1102
9	217	4.1883	0.625	0.2166	0.1584
8	169	5.6725	0.555	0.2187	0.2263
7	127	7.8112	0.458	0.2195	0.3225

If the resonant frequency of fuel elements is sufficiently low to present a seismic resonance hazard, their frequency can be increased by making fuel elements shorter and wider, increasing the width w of the system, and decreasing its height L. Frequency scales as $f \propto \sqrt{K/m}/L^2$, where the stiffness $K \propto w^4$ and mass $m \propto w^2$; therefore $f \propto w/L^2$.

The effect of the grid plate and its support structure was not included in the resonant frequency analysis in Section I.8.2.2; a comprehensive coupled seismic assessment, including the response of the grid plate and its structural support, will be a critical task for the final structural design phase.

I.3 Self-sintering Hazard

The operating temperature of ≈930 K places the homologous temperature of fuel particles, which have a solidus temperature ≈1350 K, at 0.7. At this temperature the diffusion range might be as large as 6 µm$\sqrt{t}$, where t is in hours. With turnover of five hours, self sintering might become severe. Flowing through the maze of coolant tubes in the six-bin hopper might not break the bonds, or might be impossible because of the bonds. If experiments show this is a significant hazard, several changes are possible.

- Include fluidic oscillators in the coolant tubes to produce vibrations. The amplitude needs to be in the range 20–50 µm and the acceleration needs to be in the range 0.5–2 g to exceed the yield stress of a Bingham plastic. Particle acceleration is related to frequency as

$$a = A\omega^2 \text{ or } f = \frac{\omega}{2\pi} = \frac{1}{2\pi}\sqrt{\frac{a}{A}}\,, \tag{I.1}$$

  where a is acceleration, A is amplitude, and ω is angular frequency. For 1 g acceleration with $A \approx 30$ µm, $f \approx 90$ Hz. If a single ≈90 Hz vibration does not penetrate throughout the paste between tubes, as must be determined by experiments, introduce oscillators with different frequencies in each tube. ≈90 Hz is within the range of elements' resonant frequencies (Table I.9), so oscillator frequencies must be chosen carefully.

  The in-vacuo bending stress on coolant tubes is

$$\sigma = \frac{3}{2}\frac{E\,D\,A}{L^2} \approx 12.125 \text{ kPa}\,, \tag{I.2}$$

where E is Young's modulus (194×10^9 Pa), D is tube diameter (3.125 mm), A is the vibration amplitude (30 µm) and L is tube length (1.5 m). This is well below the $\sigma_{\max} = 100$–150 MPa endurance limit for RAFM steel with 300–500 MPa tensile strength.

Whether this vibration significantly reduces fuel element life due to micro cracks, corrosion, fatigue, or abrasion, is a subject for experiments.

- Increase the turnover rate. This requires increasing the $\approx 7.8\%$ slurry velocity, which requires increasing the eductor power. Increasing turnover increases abrasion. The extent of reduction in service life, and the required increase in structural element thicknesses, are subjects for experiments.

- Use a mononitride ceramic fuel. A carbide fuel risks carburization of structural elements. The particles' centerline temperatures will be higher because of lower thermal conductivity, but their surface temperatures might be low enough that the homologous temperature is low enough to inhibit self sintering.

  Nitride fuels cannot be directly processed by the method described in Part II. They can, in principle, be reduced to metal by contact with a highly-reactive metal such as calcium. A carrier chloride salt is usually used, but alkali metals would remain in the salt, from which they would be very difficult to remove; a Borho process or fractional distillation would be necessary [7, 8]. At EBR-II salt was cleansed using Zeolyte-A, but it occluded excessive electrolyte, and did not occlude caesium well [1].

  The behavior of fission products during this process is not known. It is not likely that lanthanide nitrides will be reduced, which is perhaps an advantage. The fate of other fission products is unknown. Whether the fuel processing method described in Part II can be used is a subject for experiments. A stirred mixing process containing both cadmium and calcium, which are immiscible in the molten state over a wide mixing ratio [16, p. 605], might work — another subject for experiments.

  Zirconium is not needed to modulate the solidus temperature, and has undesirable effects on the neutron spectrum. It might be useful to add natural zirconium (not expensive hafnium-free nuclear-grade zirconium) during processing to form intermetallic compounds, although alternative additives might work.

  Rosatom has developed a hybrid pyrochemical-hydrometallurgical method for their BREST reactor. The processes are similar to the EBR-II pyroprocessor, followed by an immiscible-solvent polishing process to reduce actinide carryover to ≈ 1 ppm [41]. Alkali metal salts are removed from electrolyte by fractional distillation. The expensive ^{15}N isotope is recovered.